

Evolution of wide O star binaries through their LBV stage

Population synthesis with mass-ejection-driven orbital evolution

Xiao-Tian Xu (徐啸天)¹, Philipp Podsiadlowski^{2,3}, Norbert Langer⁴, Xue-Feng Wang⁵, Xiang-Dong Li^{6,7}, Alexander Heger⁸, Jonathan Mackey⁹, Götz Gräfen⁴, and Harim Jin^{4,10}

¹ Tsung-Dao Lee Institute, Shanghai Jiao-Tong University, 1 Lisuo Road, Shanghai, 201210, People's Republic of China
e-mail: xxu-tdli@sjtu.edu.cn

² London Institute for Stellar Astrophysics, Vauxhall, London

³ University of Oxford, St Edmund Hall, Oxford, OX1 4AR, United Kingdom

⁴ Argelander-Institut für Astronomie, Universität Bonn, Auf dem Hügel 71, 53121 Bonn, Germany

⁵ Purple Mountain Observatory, Chinese Academy of Sciences, Nanjing 210023, People's Republic of China

⁶ School of Astronomy and Space Science, Nanjing University, Nanjing, 210023, People's Republic of China

⁷ Key Laboratory of Modern Astronomy and Astrophysics, Nanjing University, Ministry of Education, Nanjing, 210023, People's Republic of China

⁸ School of Physics and Astronomy, Monash University, Vic 3800, Australia

⁹ Dublin Institute for Advanced Studies, Astronomy & Astrophysics Section, DIAS Dunsink Observatory, Dublin, D15 XR2R, Ireland

¹⁰ Max-Planck-Institut für Astrophysik, Karl-Schwarzschild-Strasse 1, 85748 Garching, Germany

Submitted date / Received date / Accepted date

ABSTRACT

Context. Long-period Wolf-Rayet (WR) star binaries produced by mass transfer are predicted to be abundant, but are observationally rare. This yields constraints on the evolution of initially wide O star binaries, including those potentially leading to the formation of gravitational-wave sources through the Common Envelope Channel.

Aims. We investigate this issue in the light of a new type of orbital evolution for initially wide O star binaries, which is driven by mass ejection at periastron passage during the Luminous Blue Variable (LBV) phase.

Methods. The assumption that the mass ejection occurs instantly at periastron passage allows us to analytically describe the orbital evolution. This approach is motivated by our understanding of an Eddington-limit driven LBV phase. We perform population synthesis calculations for the WR stars in the Small Magellanic Cloud (SMC), and compare them to the observed SMC WR star population.

Results. Different from mass transfer, our mass ejection scenario leads to increased orbital periods and eccentricities. The Galactic system WR 140 (orbital period 2895 d, eccentricity 0.9) could be a typical result of this evolution scenario. Our models predict measurable binary space velocities, and allow for the disruption of the binary. Our SMC population synthesis model predicts statistically 5.3 close, 3.7 long-period, and further 2 runaway single WR stars. With largely increased orbital periods and eccentricities, such WR+O star binaries may not be ruled out by past radial-velocity searches. Applying our scenario to the Gaia BH1 and BH2 systems, we find that it provides viable progenitor evolution models.

Conclusions. The mass-ejection-driven orbital evolution could explain why so few wide WR binaries are observed, and why some of the apparently single WR stars have high space velocities. We discuss implications for gravitational-wave sources.

Key words. Stars: evolution - Stars: massive - Stars: Wolf-Rayet - Magellanic Clouds

1. Introduction

Observations show that most massive stars have a nearby companion star (Sana et al. 2012, 2013; Moe & Di Stefano 2017; Sana et al. 2025). Hence, the evolution of isolated massive binaries may provide a natural way to produce merging binary black holes (BBHs; e.g., Belczynski et al. 2016; Marchant et al. 2021; Mandel & Broekgaarden 2022; Marchant & Bodensteiner 2024; Klencki et al. 2025; Xu et al. 2025a; Briel et al. 2026). Several evolutionary channels have been identified, including the channel involving common envelope evolution (CEE; Ivanova et al. 2013; Lau et al. 2025; Chen 2025). Whereas large uncertainties in stellar physics (Langer 2012) and mass transfer physics (Marchant & Bodensteiner 2024) impact the predicted merger rates of BBHs, the CEE channel may play a dominating role in forming merging BBHs due to the strong orbital shrinkage that

naturally in such systems (Belczynski et al. 2016; Mapelli 2020; Mandel & Broekgaarden 2022).

Figure 1 shows a schematic plot of the CEE channel for merging BBHs. The expansion of the primary star triggers the first mass transfer phase. We refer to Eldridge et al. (2017), Langer et al. (2020), Wang et al. (2020), Sen et al. (2022), Fragos et al. (2023), Xu et al. (2025b), Schürmann et al. (2025), and Jin et al. (2025) for detailed descriptions on the physics of the first mass transfer phase. The stripping of the hydrogen-rich envelope of the primary star exposes the massive helium core (He star), which can appear as a Wolf-Rayet (WR) star if massive enough¹. Then, WR stars at low metallicities usually end their lives as black holes (BH; Aguilera-Dena et al. 2023). Form-

¹ In this work, we only consider classical WR stars, which are core-helium-burning stars formed through binary-stripping or self-stripping

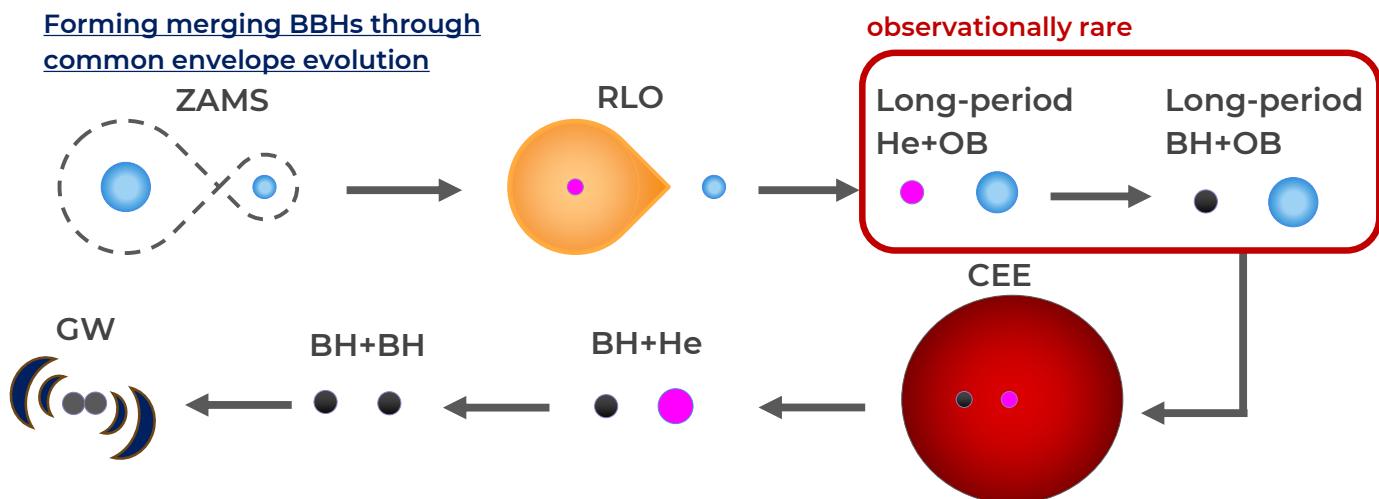


Fig. 1. Schematic evolutionary sequence for forming merging black holes through common envelope evolution from isolated massive binaries. The meaning of the abbreviations are, 1) "ZAMS" for zero-age main sequence, 2) "RLO" for Roche-lobe overflow, 3) "He" for helium star, 4) "OB" for OB-type main-sequence star, 5) "CEE" for common envelope evolution, 6) "GW" for gravitational wave. Cumulating evidence shows that the progenitors (indicated by the red box) of the CEE phase are rarer than expected in recent surveys.

ing a merging BBH in the end requires the WE- and BH-main-sequence (MS) star binaries to be wide enough to survive the CEE phase (Xu 2024; Xu et al. 2025b).

Whereas the CEE channel can reproduce various properties of the observed merging BBHs (Belczynski et al. 2016; Kruckow et al. 2018; Bavera et al. 2021; Broekgaarden et al. 2022; Olejak et al. 2024; Willcox et al. 2025), there is an increasing number of studies suggesting that long-period WR/BH-MS binaries — the progenitor systems of the CEE phase — appear to be rare, at the metallicities of the Magellanic Clouds and the Milky Way (Pauli et al. 2022; Schootemeijer et al. 2024; Deshmukh et al. 2024; Xu et al. 2025b).

For example, the observed sample of WR stars in the Small Magellanic Cloud (SMC) is thought to be complete, of which 7 appear single, 4 are WR+O binaries, and one is a WR+WR binary (Foellmi et al. 2003; Shenar et al. 2016, 2018; Schootemeijer & Langer 2018). Detailed binary evolution models well reproduce the observed four WR+O binaries (Wang et al. 2024; Xu et al. 2025b), which have orbital periods below 20 d. At the same time, Xu et al. (2025b) predict a similar number of long-period (above 20 d) WR+OB binaries. The majority of those would have been detected by the monitoring campaign of Schootemeijer et al. (2024), which excludes companions to the apparently single WR stars more massive than $5 M_{\odot}$ with period below 1 year. The Large Magellanic Cloud shows a similar lack of long-period massive evolved binaries (Langer et al. 2020; Pauli et al. 2022). A few Galactic Wolf-Rayet star binaries are observed to have long orbital periods, but their number is below the expectation of population synthesis calculations (Deshmukh et al. 2024).

One way to alleviate this problem would be to assume that most wide O star binaries merge during their mass transfer. This could happen if the mass transfer efficiency would be higher than in the models quoted above. When a mass gainer accretes a high fraction of the transferred mass, its envelope inflates (Lau et al. 2024; Schürmann & Langer 2024; Henneco et al. 2024; Wang et al. 2026), which can trigger mass overflow through the outer Lagrangian point, causing

(Shenar et al. 2020), while some WR stars are likely burning hydrogen (Gräfener & Hamann 2008; Shenar 2024).

the mass transfer to turn unstable (Schürmann & Langer 2024; Henneco et al. 2024; Scherbak et al. 2025). Population synthesis studies on Be X-ray binaries do suggest a mass transfer efficiency of about 50% (Shao & Li 2014; Vinciguerra et al. 2020; Schürmann et al. 2025; Xing et al. 2026), while a low mass transfer efficiency seems to be more suitable for more massive systems (Petrovic et al. 2005; Shao & Li 2016; Xu et al. 2025b; Schürmann et al. 2025; Zapartas et al. 2025). Schürmann et al. (2025) find that an increased mass transfer efficiency indeed predicts fewer long-period WR star binaries, but still expecting a considerable fraction of long-period systems.

In this work, we investigate an alternative scenario for the evolution of wide massive O star binaries. The Milky Way contains a small group of WR binaries with O8–O9 companions and one O5 companion (WR 140), featuring long orbital periods ($P_{\text{orb}} \sim 10$ yr) and detected through dust emission (Rosslowe & Crowther 2015; Williams 2019; Thomas et al. 2021). Three of them have eccentricity (e) measurements, WR 140 ($e: 0.8993$, $P_{\text{orb}}: 2895$ d; Thomas et al. 2021), WR 19 ($e: 0.8$, $P_{\text{orb}}: 10.1$ yr; Williams et al. 2009), and WR 137 ($e: 0.18$, $P_{\text{orb}}: 13.05$ yr; Lefèvre et al. 2005). If such WR 140-like systems also exist in the Magellanic Clouds, they might remain undetected binaries based on past radial velocity variability searches (Foellmi et al. 2003; Hainich et al. 2014; Schootemeijer et al. 2024). If they avoided the WC phase, also episodic dust production would not occur.

At the same time, the observed properties of WR 140 can hardly be explained by current binary evolution models. The orbital separation of WR 140 at periastron is about $293 R_{\odot}$, suggesting that past strong binary interaction was inevitable. When the progenitor of the WR star approaches Roche-lobe filling, current binary evolution models expect the orbit to be circularised efficiently (e.g., Verbunt & Phinney 1995; Hurley et al. 2002; Belczynski et al. 2008; Kruckow et al. 2018; Fragos et al. 2023), and the following mass transfer phase does not induce eccentricities either (Tauris & van den Heuvel 2006, 2023; Marchant & Bodensteiner 2024). It is also proposed that mass transfer may occur in eccentric binaries, which can enhance the eccentricity instead of circularisation (Sepinsky et al. 2007; Rocha et al. 2025; Parkosidis et al. 2025a,b). While this scenario can reproduce the observed eccentricities of evolved low-mass

binaries (Parkosidis et al. 2025a), it cannot explain the proper motion velocity of WR 140 ($\sim 34 \text{ km s}^{-1}$; Dzib & Rodríguez 2009).

As the primary stars in wide Ostar binaries can expand considerably, they may reach their Eddington limit and turn into LBVs before mass transfer is initiated. We propose that the orbital evolution of such binaries is then driven by the mass ejection during the luminous blue variable (LBV) phase of the primary stars instead of the mass transfer through Roche-lobe overflow. While this has been suggested before (e.g., Vanbeveren 1991; Bavera et al. 2023; Willcox et al. 2025; Olejak et al. 2025), it was applied to circular binaries. We will show that, if this mass ejection preferentially occurs at periastron, it efficiently increases orbital periods, enhances eccentricities, produces measurable space velocities, and even causes binary disruption if the pre-mass-ejection binary has a large eccentricity.

This paper is organised as follows. We derive the equations for the mass-ejection-driven orbital evolution and introduce our method for population synthesis in Sect. 2. In Sect. 3, we present example models for the mass-ejection-driven orbital evolution, the application to WR 140, and population synthesis predictions for the WR stars in the SMC. We compare with observations and discuss the implications and uncertainties of our model in Sect. 4. We summarise our work in Sect. 5.

2. Model and method

In this section, we derive the equations for the mass-ejection-driven orbital evolution (Sect. 2.1). Then, we introduce our method for population synthesis calculations (Sect. 2.2).

2.1. Mass ejection driven orbital evolution

We assume that the mass-ejection-driven orbital evolution takes place when the primary star enters its LBV phase. As at this stage the binary orbit is likely to still be eccentric, we expect the primary will approach Roche lobe filling at periastron passage. Here, we assume that the loosely bound inflated envelope of the primary star can be kicked off instantly at periastron passage, with tidal effects on the orbital period and separation being negligible. We discuss in detail the trigger mechanism of this periastron mass ejection in Sect. 4.5. A similar process has been proposed for asymptotic giant branch stars, whose mass loss rate can be enhanced by tidal interaction in binaries, producing eccentricities (Soker 2000; Bonačić Marinović et al. 2008; Vos et al. 2015). While our assumption is certainly an oversimplification of the situation, it allows an analytic prescription of the further evolution which might still capture the main features in such events. For primary stars which are not massive enough to reach the LBV phase, we assume that its dense envelope allows for tidal circularisation and ordinary Roche-lobe overflow evolution.

We first investigated the dynamical effect of one sudden mass ejection at periastron, which has been discussed previously (Blaauw 1961; Hills 1983; Tauris & Takens 1998; van den Heuvel et al. 2000; Hurley et al. 2002; Pfahl et al. 2002). In this work, we extended the analysis by Hills (1983), and we calculated the orientation of the post-mass-ejection orbit with the coordinate-independent description provided in Pfahl et al. (2002). Then, we establish the equations for long-term orbital evolution. For completeness, we also present the orbital-evolution equations for mass ejections occurring at apastron in App. A.

2.1.1. Pre-mass-ejection orbit

The two-body problem (i.e., the Kepler problem) well describes the properties of the pre-mass-ejection orbit. Considering a binary system with stellar components having masses of M_{s1} ("s1" for star 1, the primary star) and M_{s2} ("s2" for star 2, the secondary star), the velocity of the centre of mass, $v_{\text{CoM},0}$, is defined as

$$M_{s1} \vec{v}_{s1} + M_{s2} \vec{v}_{s2} = M_{b,0} \vec{v}_{\text{CoM},0}, \quad (1)$$

where $M_{b,0}$ is the total mass of the binary (i.e., $M_{s1} + M_{s2}$), where the subscript "0" indicates the value before the mass ejection event, v_{s1} and v_{s2} are the velocities of star 1 and star 2, and the relative velocity, v_0 , is defined as

$$\vec{v}_{s1} - \vec{v}_{s2} = \vec{v}_0, \quad (2)$$

and the space velocities of the stellar components are given by

$$\vec{v}_{s1} = \vec{v}_{\text{CoM},0} + \frac{M_{s2}}{M_{b,0}} \vec{v}_0, \quad (3)$$

and

$$\vec{v}_{s2} = \vec{v}_{\text{CoM},0} - \frac{M_{s1}}{M_{b,0}} \vec{v}_0. \quad (4)$$

The orbital energy, E_0 , is given by

$$E_0 = -G \frac{M_{s1} M_{s2}}{r} + \frac{1}{2} \mu_0 v_0^2 = -G \frac{M_{s1} M_{s2}}{2a_0}, \quad (5)$$

or equivalently

$$\frac{E_0}{\mu_0} = -G \frac{M_{b,0}}{r} + \frac{1}{2} v_0^2 = -G \frac{M_{b,0}}{2a_0}, \quad (6)$$

where G is the gravitational constant, r is the orbital separation, μ_0 is the reduced mass, which is $\mu_0 = M_{s1} M_{s2} / M_{b,0}$, and a_0 is the semi-major axis. The orbital angular momentum, J_0 , is given by

$$|\vec{J}_0| = \mu_0 |\vec{r} \times \vec{v}_0| = \mu_0 \sqrt{GM_{b,0} a_0 (1 - e_0^2)}, \quad (7)$$

where e_0 is the eccentricity. The orbital separation can also be expressed as a function of true anomaly, θ , which is

$$r = \frac{a_0 (1 - e_0^2)}{1 + e_0 \cos \theta}. \quad (8)$$

The separation at periastron is evaluated by taking $\theta = 0$,

$$r_{\text{per},0} = a_0 (1 - e_0). \quad (9)$$

Combining Eqs. (9) with (5), we obtained the relative velocity at periastron,

$$v_{\text{per},0} = \sqrt{\frac{GM_{b,0}}{a_0} \frac{1 + e_0}{1 - e_0}} = \left(\frac{GM_{b,0}}{P_{\text{orb},0}} 2\pi \right)^{1/3} \sqrt{\frac{1 + e_0}{1 - e_0}}, \quad (10)$$

where a_0 was replaced by the orbital period, $P_{\text{orb},0}$, through the Kepler's third law,

$$\left(\frac{2\pi}{P_{\text{orb},0}} \right)^2 a_0^3 = GM_{b,0}. \quad (11)$$

In addition, we introduced an additional parameter to measure the detectability of a given binary system through radial velocity measurements, which is the orbital-period-averaged relative velocity,

$$\begin{aligned} \langle v_{\text{orb}} \rangle &= \int_0^{P_{\text{orb}}} \frac{v_0}{P_{\text{orb},0}} dt = \int_0^{2\pi} \frac{v_0}{P_{\text{orb},0}} \frac{dt}{d\theta} d\theta \\ &= \int_0^{2\pi} \frac{v_0}{P_{\text{orb},0} \omega_{\text{orb}}} d\theta, \end{aligned} \quad (12)$$

where t is the evolutionary time, θ is the true anomaly in Eq. (8), and ω_{orb} is the Keplerian angular velocity, which is

$$\omega_{\text{orb}} = \frac{\sqrt{GM_{\text{b},0} a_0 (1 - e_0^2)}}{r^2}. \quad (13)$$

Combining Eqs. (5), (8), and (13) with Eq. (12), we obtained

$$\begin{aligned} \langle v_{\text{orb}} \rangle &= 2 \frac{a_0(1 - e_0^2)}{P_{\text{orb},0}} \int_0^\pi \sqrt{\frac{1 + 2e_0 \cos \theta + e_0^2}{(1 + e_0 \cos \theta)^4}} d\theta \\ &= 4 \frac{a_0}{P_{\text{orb},0}} \int_0^{\pi/2} \sqrt{1 - e_0^2 \sin^2 \phi} d\phi \\ &= 4 \frac{a_0}{P_{\text{orb},0}} I(e_0) = 4 \left[\frac{GM_{\text{b},0}}{4\pi^2 P_{\text{orb},0}} \right]^{1/3} I(e_0), \end{aligned} \quad (14)$$

where the elliptic integral,

$$I(e_0) = \int_0^{\pi/2} \sqrt{1 - e_0^2 \sin^2 \phi} d\phi, \quad (15)$$

cannot be solved analytically (Murray & Dermott 1999). Hence, we applied an empirical formula to fit the numerical solution of Eq. (15) (Abramowitz & Stegun 1972), which is

$$I(e) \simeq C_1 + C_2 e + C_3 e^2 + C_4 e^3 + C_5 e^4, \quad (16)$$

where

$$\begin{cases} C_1 = 1.56690314 \\ C_2 = 0.10180252 \\ C_3 = -0.97975648 \\ C_4 = 1.16831992 \\ C_5 = -0.83659936 \end{cases}. \quad (17)$$

Figure 2 compares our fitting formula and the numerical solution. Then, the averaged orbital velocity in the centre-of-mass frame of the mass-losing star is given by

$$\langle v_{\text{s}1} \rangle = \frac{M_{\text{s}2}}{M_{\text{b},0}} \langle v_{\text{orb}} \rangle. \quad (18)$$

In addition, the orbital velocities in the centre-of-mass frame of the mass-losing star at periastron and apastron are

$$v_{\text{s}1,\text{per}} = \frac{M_{\text{s}2}}{M_{\text{b},0}} v_{\text{per},0} \quad (19)$$

and

$$v_{\text{s}1,\text{ap}} = \frac{M_{\text{s}2}}{M_{\text{b},0}} v_{\text{ap},0}, \quad (20)$$

where $v_{\text{ap},0}$ is the relative velocity at apastron (Eq. A.1).

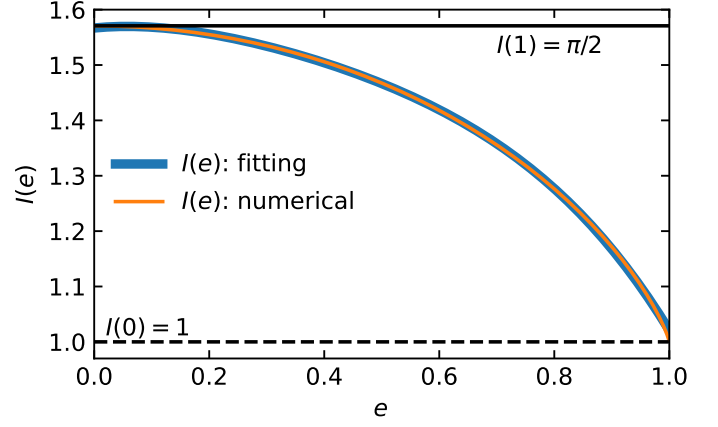


Fig. 2. Comparison between our fitting formula (blue curve; Eq. 16) and the numerical solution of Eq. (15) (orange curve). The black solid and dashed lines represent $I(1) = \pi/2$ and $I(0) = 1$.

2.1.2. Post-mass-ejection orbit

For analytical simplicity, we adopted the following assumptions on the sudden mass ejection at periastron, consistent with previous works (Hills 1983; Tauris & Takens 1998; Pfahl et al. 2002):

1. the mass ejection is isotropic and does not induce additional momentum kicks on the mass-losing star (see Hills 1983, Tauris & Takens 1998, and Pfahl et al. 2002 for the effect of significant momentum kicks in supernova explosions);
2. the mass ejection is a delta function in time (cf. Sect. 4.5);
3. the effect of the tidal torque is ignorable;
4. the velocity of the centre of mass of the pre-mass-ejection system is zero (i.e., $v_{\text{CoM},0} = 0$);
5. the binary system does not undergo apsidal advance or precession induced for external reasons (cf. Sect. 4.6 and App. F).

We assumed that the ejection event takes away a mass of ΔM , while the mass of the secondary star remains unchanged. According to our sudden ejection assumption, the relative velocity, space velocities², and orbital separation remain unchanged right after the ejection. Hence the post-mass-ejection orbital energy is given by

$$-G \frac{M_{\text{b},0} - \Delta M}{r_{\text{per},0}} + \frac{1}{2} v_{\text{per},0}^2 = -G \frac{M_{\text{b},0} - \Delta M}{2a_1}, \quad (21)$$

where a_1 is the semi-major axis of the post-mass-ejection orbit, and the subscript "1" indicates the value after mass ejection. The post-ejection orbital angular momentum is

$$J_1 = \mu_1 |\vec{r}_{\text{per},0} \times \vec{v}_{\text{per},0}| = \mu_1 \sqrt{G(M_{\text{b},0} - \Delta M) a_1 (1 - e_1^2)}, \quad (22)$$

where $\mu_1 = (M_{\text{s}1} - \Delta M) M_{\text{s}2} / (M_{\text{b},0} - \Delta M)$, and e_1 is the post-mass-ejection eccentricity. The post-mass-ejection orbital period, $P_{\text{orb},1}$, is given by Kepler's third law,

$$P_{\text{orb},1}^2 = \frac{(2\pi)^2 a_1^3}{G(M_{\text{b},0} - \Delta M)}. \quad (23)$$

² The orbital velocities in the centre-of-mass frame do change because of the changes in masses (Eqs. 19 and 20). It can be shown that

$$\vec{v}_{\text{s}1} = \frac{M_{\text{s}2}}{M_{\text{b},0}} \vec{v}_{\text{per},0} = \frac{M_{\text{s}2}}{M_{\text{b},0} - \Delta M} \vec{v}_{\text{per},0} + \vec{v}_{\text{CoM},1},$$

which is consistent with our assumption.

Combining the above equations, we obtained the properties of the post-mass-ejection orbit,

$$a_1 = a_0(1 - e_0) \frac{M_{b,0} - \Delta M}{M_{b,0}(1 - e_0) - 2\Delta M}, \quad (24)$$

$$e_1 = \frac{\Delta M + e_0 M_{b,0}}{M_{b,0} - \Delta M}, \quad (25)$$

$$P_{\text{orb},1}^2 = P_{\text{orb},0}^2 \frac{(1 - \Delta M/M_{b,0})^2(1 - e_0)^3}{[(1 - e_0) - 2\Delta M/M_{b,0}]^3}. \quad (26)$$

Due to angular-momentum conservation, the change of mass causes a momentum kick on the centre of mass,

$$(M_{s1} - \Delta M)\vec{v}_{s1} + M_{s2}\vec{v}_{s2} = (M_{b,0} - \Delta M)\vec{v}_{\text{CoM},1}, \quad (27)$$

which gives the post-mass-ejection velocity of the centre of mass,

$$\vec{v}_{\text{CoM},1} = \vec{v}_{\text{CoM},0} - \frac{\Delta M M_{s2}}{M_{b,0}(M_{b,0} - \Delta M)} \vec{v}_{\text{per},0}, \quad (28)$$

which shows that the momentum kick has the opposite direction to $\vec{v}_{\text{per},0}$. As we assumed that the initial velocity of the centre of mass is zero, the magnitude of $\vec{v}_{\text{CoM},1}$ is

$$v_{\text{CoM},1} = \frac{\Delta M M_{s2}}{M_{b,0}(M_{b,0} - \Delta M)} v_{\text{per},0}. \quad (29)$$

These equations imply that a mass ejection at periastron makes the post-mass-ejection orbit wider and more eccentric. Setting $e_1 = 1$, we find that the amount of the ejected mass required for binary disruption is

$$\Delta M_{\text{dis}} = \frac{1}{2} M_{b,0}(1 - e_0), \quad (30)$$

which is consistent with Hills (1983). In addition, we note that the post-mass-ejection orbit meets the following condition,

$$a_1(1 - e_1) = r_{\text{per},0} = a_0(1 - e_0), \quad (31)$$

which means that the separation at periastron remains unchanged. While the orbit of the binary is no longer closed due to the mass ejection, the orientation of the post-mass-ejection orbit stays the same as the pre-mass-ejection orbit. In the following, we demonstrate this by considering the Laplace-Runge-Lenz vector³, which is

$$\begin{aligned} \vec{e}_0 &= \frac{\vec{v}_{\text{per},0} \times (\vec{r}_{\text{per},0} \times \vec{v}_{\text{per},0})}{GM_{b,0}} - \frac{\vec{r}_{\text{per},0}}{r_{\text{per},0}} \\ &= \frac{v_{\text{per},0}^2 \vec{r}_{\text{per},0} - (\vec{r}_{\text{per},0} \cdot \vec{v}_{\text{per},0}) \vec{v}_{\text{per},0}}{GM_{b,0}} - \frac{\vec{r}_{\text{per},0}}{r_{\text{per},0}}, \end{aligned} \quad (32)$$

where $\vec{r}_{\text{per},0}$ is the vector pointing from the secondary star to the mass-losing star. At periastron, $\vec{r}_{\text{per},0}$ is perpendicular to $\vec{v}_{\text{per},0}$, which gives

$$\vec{r}_{\text{per},0} \cdot \vec{v}_{\text{per},0} = 0. \quad (33)$$

Hence, the Laplace-Runge-Lenz vector before the mass ejection is

$$\vec{e}_0 = \frac{v_{\text{per},0}^2 \vec{r}_{\text{per},0}}{GM_{b,0}} - \frac{\vec{r}_{\text{per},0}}{r_{\text{per},0}} = \left[\frac{v_{\text{per},0}^2}{GM_{b,0}} - \frac{1}{r_{\text{per},0}} \right] \vec{r}_{\text{per},0}, \quad (34)$$

³ The definition is given by Eq. (B1) in Pfahl et al. (2002).

which has the same orientation as $\vec{r}_{\text{per},0}$, as expected. After the mass ejection, the Laplace-Runge-Lenz vector becomes

$$\vec{e}_1 = \left[\frac{v_{\text{per},0}^2}{G(M_{b,0} - \Delta M)} - \frac{1}{r_{\text{per},0}} \right] \vec{r}_{\text{per},0}. \quad (35)$$

It is clear that $M_{b,0} - \Delta M < M_{b,0}$, which leads to the following strict inequality,

$$\begin{aligned} \frac{v_{\text{per},0}^2}{G(M_{b,0} - \Delta M)} - \frac{1}{r_{\text{per},0}} &> \frac{v_{\text{per},0}^2}{GM_{b,0}} - \frac{1}{r_{\text{per},0}} \\ &= \frac{e_0}{a_0(1 - e_0)} > 0. \end{aligned} \quad (36)$$

Therefore, we obtained

$$\begin{cases} \vec{e}_0 \times \vec{e}_1 \propto \vec{r}_{\text{per},0} \times \vec{r}_{\text{per},0} = 0 \\ \vec{e}_0 \cdot \vec{e}_1 = |\vec{e}_0 \cdot \vec{e}_1| \end{cases}, \quad (37)$$

which means that the orientation of the post-mass-ejection orbit has the same orientation as the pre-mass-ejection orbit⁴.

2.1.3. Long-term orbital evolution

Based on our result on one mass ejection at periastron, in this section we derive the orbital-evolution equations by considering that the LBV primary star experiences a series of mass ejection events associated with periastron passages, and the amount of ejected mass during each periastron passage was fixed to be ΔM .

Letting $(a_1, e_1, P_{\text{orb},1}, v_{\text{CoM},1})$ be the orbital parameters after the first periastron passage, and the binary mass becomes $(M_{b,0} - \Delta M)$. Since the separation and orientation of periastron remains unchanged (Eqs. 31 and 37), we can obtain the parameters after the second mass ejection, $(a_2, e_2, P_{\text{orb},2}, v_{\text{CoM},2})$, by replacing $M_{b,0}$ in Eqs. (24)–(26) and (29) with $(M_{b,0} - \Delta M)$,

$$\begin{aligned} a_2 &= a_1(1 - e_1) \frac{(M_{b,0} - \Delta M) - \Delta M}{(M_{b,0} - \Delta M)(1 - e_1) - 2\Delta M} \\ &= a_0(1 - e_0) \frac{M_{b,0} - 2\Delta M}{M_{b,0}(1 - e_1) - 2(2\Delta M)}, \end{aligned} \quad (38)$$

$$\begin{aligned} e_2 &= \frac{\Delta M + e_1(M_{b,0} - \Delta M)}{(M_{b,0} - \Delta M) - \Delta M} \\ &= \frac{(2\Delta M) + e_0 M_{b,0}}{M_{b,0} - (2\Delta M)}, \end{aligned} \quad (39)$$

$$\begin{aligned} P_{\text{orb},2}^2 &= P_{\text{orb},1}^2 \frac{[1 - \Delta M/(M_{b,0} - \Delta M)]^2(1 - e_1)^3}{[(1 - e_1) - 2\Delta M/(M_{b,0} - \Delta M)]^3} \\ &= P_{\text{orb},0}^2 \frac{(1 - 2\Delta M/M_{b,0})^2(1 - e_0)^3}{[(1 - e_0) - 2(2\Delta M)/M_{b,0}]^3}, \end{aligned} \quad (40)$$

$$\begin{aligned} v_{\text{CoM},2} &= v_{\text{CoM},1} + \frac{\Delta M M_{s2}}{(M_{b,0} - \Delta M)[(M_{b,0} - \Delta M) - \Delta M]} v_{\text{per},0} \\ &= \frac{(2\Delta M)M_{s2}}{M_{b,0}(M_{b,0} - 2\Delta M)} v_{\text{per},0}. \end{aligned} \quad (41)$$

The above equations are consistent with the expectation of Eqs. (24)–(26) and (29) if the ejected mass is taken to be $2\Delta M$

⁴ If the mass ejection occurs at apastron, the pre-mass-ejection apastron can become the periastron of the post-mass-ejection orbit (i.e., $\vec{e}_0 \cdot \vec{e}_1 = -|\vec{e}_0 \cdot \vec{e}_1|$; see App. A), depending on the ejected mass.

during one periastron passage, which means that the orbital parameters are determined by the initial orbital parameters, $(a_0, e_0, P_{\text{orb},0}, v_{\text{CoM},0})$, and the total amount of ejected mass. If the binary stays bound, this is also true for the parameters after the n th periastron passage, $(a_n, e_n, P_{\text{orb},n}, v_{\text{CoM},n})$, which are

$$a_n = a_0(1 - e_0) \frac{M_{\text{b},0} - n\Delta M}{M_{\text{b},0}(1 - e_0) - 2n\Delta M}, \quad (42)$$

$$e_n = \frac{n\Delta M + e_0 M_{\text{b},0}}{M_{\text{b},0} - n\Delta M}, \quad (43)$$

$$P_{\text{orb},n}^2 = P_{\text{orb},0}^2 \frac{(1 - n\Delta M/M_{\text{b},0})^2(1 - e_0)^3}{[(1 - e_0) - 2n\Delta M/M_{\text{b},0}]^3}, \quad (44)$$

$$v_{\text{CoM},n} = \frac{n\Delta M M_{\text{s}2}}{M_{\text{b},0}(M_{\text{b},0} - n\Delta M)} v_{\text{per},0}, \quad (45)$$

where $n\Delta M$ represents the total ejected mass. In App B, we prove this using mathematical induction. Hence, if a binary enters the mass-ejection-driven orbital evolution, the orbital parameters at the end of the evolution are determined by the mass of the hydrogen-rich envelope of the LBV primary star, instead of the history of the mass ejections. Correspondingly, the orbital period, space velocity, average orbital velocity, and eccentricity of the resulting WR+O binary should be correlated through the ejected mass, which leads to the following relations,

$$P_{\text{orb},n}^2 = P_{\text{orb},0}^2 \left(\frac{1 + e_n}{1 + e_0} \right) \left(\frac{1 - e_0}{1 - e_n} \right)^3, \quad (46)$$

$$v_{\text{CoM},n} = \frac{M_{\text{s}2}}{M_{\text{b},0}} \left(\frac{e_n - e_0}{1 + e_0} \right) v_{\text{per},0}, \quad (47)$$

and

$$\langle v_{\text{orb}} \rangle = 4 \left[\frac{GM_{\text{b},n}}{4\pi^2 P_{\text{orb},0}} \right]^{1/3} I(e_n) \left(\frac{1 + e_0}{1 + e_n} \right)^{1/6} \left(\frac{1 - e_n}{1 - e_0} \right)^{1/2}. \quad (48)$$

Binary disruption occurs when orbital energy is equal to or exceeds zero (i.e., $e_n \geq 1$). In the following, we derive the runaway velocities of the stellar components, which are defined as the space velocities when the separation of two components is infinite. According to the equations in Pfahl et al. (2002), the runaway velocities, $\vec{v}_{\text{s}1,\infty}$ and $\vec{v}_{\text{s}2,\infty}$, are evaluated by

$$\vec{v}_{\text{s}1,\infty} = \frac{M_{\text{s}2,\text{dis}}}{M_{\text{b},\text{dis}}} \vec{v}_{\infty} + \vec{v}_{\text{CoM},\text{dis}}, \quad (49)$$

and

$$\vec{v}_{\text{s}2,\infty} = -\frac{M_{\text{s}1,\text{dis}}}{M_{\text{b},\text{dis}}} \vec{v}_{\infty} + \vec{v}_{\text{CoM},\text{dis}}, \quad (50)$$

where "dis" indicates that the parameters are evaluated at disruption, and \vec{v}_{∞} is the relative velocity at infinite separation. In the case of a supernova explosion, the asymmetric ejecta generates a strong momentum kick on the newborn compact object (Janka 2017). Consequently, the remnant of the exploding star moves at a velocity close to the kick velocity, while the companion star has a velocity close to its orbital velocity at explosion (Hills 1983; Tauris & Takens 1998; Pfahl et al. 2002). However, binary disruption occurs in a different way in our mass-ejection-driven orbital evolution where the eccentricity increases gradually with each periastron passage. When disruption occurs, the eccentricity should be equal to or slightly above 1, and the orbital energy should be very close to zero. Then, in the centre-of-mass frame,

we have the following relation for the kinetic energy, E_{kin} , and potential energy, E_{grav} , of the system at disruption,

$$E_{\text{kin}} + E_{\text{grav}} = 0, \quad (51)$$

which suggests that, at infinite separation (i.e., $E_{\text{grav}} = 0$), the relative velocity is zero, and, according to Eqs. (49) and (50), the runaway velocities of both stars are equal to the velocity of the centre of mass at disruption, $\vec{v}_{\text{CoM},\text{dis}}$. By inserting Eq. (30) into Eq. (45), or setting $e_n = 1$ in Eq. (47), we obtained

$$v_{\text{CoM},\text{dis}} = \frac{M_{\text{s}2}}{M_{\text{b},0}} \left(\frac{1 - e_0}{1 + e_0} \right) v_{\text{per},0} = v_{\text{s}1,\infty} = v_{\text{s}2,\infty}. \quad (52)$$

2.2. Population synthesis method

Our population synthesis calculations were based on Eqs. (42)–(45), and Eq. (52), where $n\Delta M$ was set equal to the hydrogen-rich envelope of the primary star, $M_{\text{b},0}$ is taken to be the binary mass and $P_{\text{orb},0}$ the orbital period on the zero-age main sequence (ZAMS), respectively. We ignored the effects of steady stellar winds. We adopted a dense grid of detailed binary evolution models computed with a metallicity tailored for the SMC and the SMC WR star population derived from it as inputs (see Xu et al. 2025b, for the details of the binary evolution models), where the WR stars were defined as core-helium-burning stars with luminosities above $10^{5.6} L_{\odot}$ based on observations (Shenar et al. 2020). We adopted the WR star mass, M_{WR} , derived by Xu et al. (2025b), and calculated the mass of the hydrogen-rich envelope by $n\Delta M = M_{\text{ZAMS}} - M_{\text{WR}}$, where M_{ZAMS} is the ZAMS mass of the WR star.

In order to determine the occurrence of the mass-ejection-driven orbital evolution, we introduced the following criterion. The mass-ejection-driven orbital evolution is assumed to occur if the initial primary mass exceeds a critical value, M_{crit} , and simultaneously the initial orbital period is longer than a critical value, P_{crit} . The physical motivation is that, for mass ejection to occur, the primary star needs to be massive enough to enter an LBV phase by reaching its Eddington limit, and the orbit needs to be wide enough to contain an inflated star. For our Simulation1, we take $M_{\text{crit}} = 30 M_{\odot}$ and $P_{\text{crit}} = 40$ d. The luminosity of a $30 M_{\odot}$ star at the terminal-age main sequence is about $10^{5.4} L_{\odot}$ (Xu et al. 2025b), which is consistent with the observed minimal luminosity of LBVs (Smith et al. 2004; Vink 2012; Smith 2017b; Smith et al. 2019), and the adopted 40 d for P_{crit} is consistent with the inferred orbital period of the progenitor of WR 140 (cf., Sect. 3.2). For systems in which the above criteria are not met, we adopt the orbital periods for WR+O binaries obtained by Xu et al. (2025b).

Consistent with the fiducial population synthesis model in Xu et al. (2025b), we assumed that the initial primary mass, $M_{1,i}$, follows the initial mass function,

$$f_{\text{IMF}} \propto M_{1,i}^{-\alpha}, \quad (53)$$

where $\alpha = 2.3$ for massive stars (Kroupa 2001), and we adopted the initial mass ratio, f_{q_i} , and orbital period, $f_{\log P_{\text{orb},i}}$, functions in Sana et al. (2012), which are

$$f_{q_i} \propto q_i^{-0.1}, \quad (54)$$

and

$$f_{\log P_{\text{orb},i}} \propto (\log P_{\text{orb},i})^{-0.55}. \quad (55)$$

In addition to Xu et al. (2025b), we further took into account the initial eccentricity function,

$$f_e \propto e^{-\eta} \quad (56)$$

We take $\eta = 0.5$ for our Simulation1 according to the empirical eccentricity function in Sana et al. (2012). The normalisation factor of the f_e function is $(-\eta + 1)$. Hence the fraction of the binaries having eccentricities in $[e_1, e_2]$ is given by

$$\int_{e_1}^{e_2} f_e \, de = e_2^{-\eta+1} - e_1^{-\eta+1}. \quad (57)$$

The predicted number of each binary system was evaluated by a statistical weight,

$$N \propto \text{SFR} \times \text{lifetime} \times f_{\text{IMF}} f_{q_i} f_{\log P_{\text{orb},i}} f_e, \quad (58)$$

where "SFR" is the star formation rate, "lifetime" is the lifetime of the WR star in a WR+O binary, which was derived in Xu et al. (2025b). We refer to Appendix E in Xu et al. (2025b) for the details of this method. In order to better reproduce the observed number of the SMC WR stars, we adopted a higher SFR of $0.0821 M_{\odot} \text{ yr}^{-1}$ than the value of $0.05 M_{\odot} \text{ yr}^{-1}$ used in Xu et al. (2025b). With this higher SFR, we re-derived the WR star population from the fiducial population synthesis model in Xu et al. (2025b) for comparison purposes (hereafter Simulation2).

In this work, we defined runaway WR stars as the WR stars formed in disrupted binaries, regardless of their space velocities. Binary disruption can take place only if ΔM_{dis} is lower than the envelope mass of the primary star, which means that the primary star is partially stripped at disruption. We simply assumed that, after disruption, the runaway primary star ejects the remaining envelope within an ignorable timescale.

3. Results

We first present example models of the mass-ejection-driven orbital evolution to illustrate the main features of the evolution (Sect. 3.1), and we apply our model to WR 140 to infer the properties of its progenitor system (Sect. 3.2). We present our population synthesis predictions for the SMC WR stars in Sect. 3.3.

3.1. Example models

In the classical theory of orbital evolution, mass transfer redistributes the masses and angular momenta of stellar components, accompanied by mass loss, carrying away orbital angular momentum (Tauris & van den Heuvel 2006, 2023; Marchant & Bodensteiner 2024). This process does not alter the velocity of the centre of mass, and the orbit is expected to stay circularised due to the strong tidal torque for a Roche-lobe filling donor. In contrast, the mass-ejection-driven orbital evolution leads to a rapid increase in the orbital period, accompanied by an efficient increase in eccentricity. Also, the sudden mass ejections impart momentum kicks on the binary system, producing measurable space velocities.

Figure 3 presents three examples of mass-ejection-driven orbital evolution. The pre-mass-ejection orbital periods were taken to be 10 d, 100 d, and 1000 d. The initial total mass of the binaries was fixed to be $54 M_{\odot}$ with an initial mass ratio of 0.8 (i.e., $30 M_{\odot}$ primary + $24 M_{\odot}$ secondary). We assumed that each mass ejection event removes $10^{-3} M_{\odot}$, which appears achievable for LBVs (Vink & de Koter 2002; Smith & Owocki 2006; Gräfener et al. 2012; Smith 2014; Sanyal et al. 2015; Campagnolo et al. 2018;

Grassitelli et al. 2021; Cheng et al. 2024; Pauli et al. 2026). We considered two initial eccentricities, 0 (left column) and 0.3 (right column). We marked three specific values, which are $P_{\text{orb}} = 10^4$ d (a period that cannot be excluded by past $\Delta R V$ searches; see Fig. 6 in Schootemeijer et al. 2024), $e = 0.9$ (the eccentricity of WR 140; Williams 2019; Thomas et al. 2021), and $v_{\text{CoM}} = 80 \text{ km s}^{-1}$ (the peculiar velocity of the runaway WR stars in the SMC; Schootemeijer et al. 2024). We computed these models until binary disruption for presentation purpose, while, in a realistic binary evolution model, the termination point of the mass-ejection-driven orbital evolution is determined by the stripping of the hydrogen-rich envelope of the LBV primary star.

Closer binaries evolve faster due to a higher frequency of periastron passages. Our example models with circular initial orbits take about $0.07\text{--}1.21 \times 10^5$ yr to reach $P_{\text{orb}} = 10^4$ d for $P_{\text{orb},0}$ varying from 10 d to 1000 d, and the corresponding mass ejection fraction, $\Delta M/M_{\text{b},0}$, is about 0.49–0.42. Meanwhile, all models reach $e = 0.9$ at $\Delta M/M_{\text{b},0} = 0.47$, as the evolution of eccentricity does not depend on orbital period (Eq. 43). Since v_{CoM} is proportional to the relative velocity at periastron, which remains unchanged during the evolution, a closer initial orbit achieves a higher v_{CoM} at the same $\Delta M/M_{\text{b},0}$. The v_{CoM} at disruption are 165 km s^{-1} , 77 km s^{-1} , and 35 km s^{-1} , corresponding to initial orbital periods of 10 d, 100 d, and 1000 d, where only the model with $P_{\text{orb},0} = 10$ d reaches close to 80 km s^{-1} when the primary star loses half of its initial mass. The average orbital velocities of the mass-losing stars decrease with the increasing orbital periods, which are below $\sim 10 \text{ km s}^{-1}$ when reaching $P_{\text{orb}} = 10^4$ d. Given that the orbits are highly eccentric, the mass-losing stars should move more slowly than the average velocities most of the time.

Binaries with higher initial eccentricities are more easily disrupted. According to Eq. (30), it requires a $\Delta M/M_{\text{b},0}$ of 50% to disrupt an initially circular system, which is only 35% in the case of $e_0 = 0.3$. Consequently, the models with $e_0 = 0.3$ reach $P_{\text{orb}} = 10^4$ d and $e = 0.9$ at a much lower $\Delta M/M_{\text{b},0}$. Initially eccentric binaries also have higher space velocities at the same $\Delta M/M_{\text{b},0}$ due to the difference in the relative velocities at periastron (Eq. 10). Hence, if the observed runaway WR stars in the SMC were formed through the mass-ejection-driven orbital evolution, the progenitor systems were likely to be very eccentric.

The typical lifetime of an LBV is about a few 10^4 yr (Humphreys & Davidson 1994; Smith 2014). The envelope mass of a massive star at the SMC metallicity is about half of the ZAMS mass of the star (Xu et al. 2025b). For an initial mass ratio of 0.8, the primary star ejects half of its initial mass at $\Delta M/M_{\text{b},0} \approx 38.5\%$ (red stars in Fig. 3), which occurs within a few percent of the time needed for binary disruption. Meanwhile, the mass ejected during one periastron passage could be much higher than the value we assumed. A stronger mass ejection at periastron can significantly reduce the evolutionary timescale. Observationally, there are records for much more eruptive events, like the 1600 AD eruption of P Cygni ($0.1 M_{\odot}$ ejected; Smith & Hartigan 2006), and the Great Eruption of η Carinae in the 19th century ($10 M_{\odot}$ ejected; Smith et al. 2003). Therefore, the proposed mass-ejection-driven orbital evolution does not contradict the lifetime of LBVs.

3.2. The progenitor of WR 140

Since the final orbital parameters of the mass-ejection-driven orbital evolution only depends on the total ejected mass (i.e., the hydrogen-rich envelope of the mass-losing star), it can be used

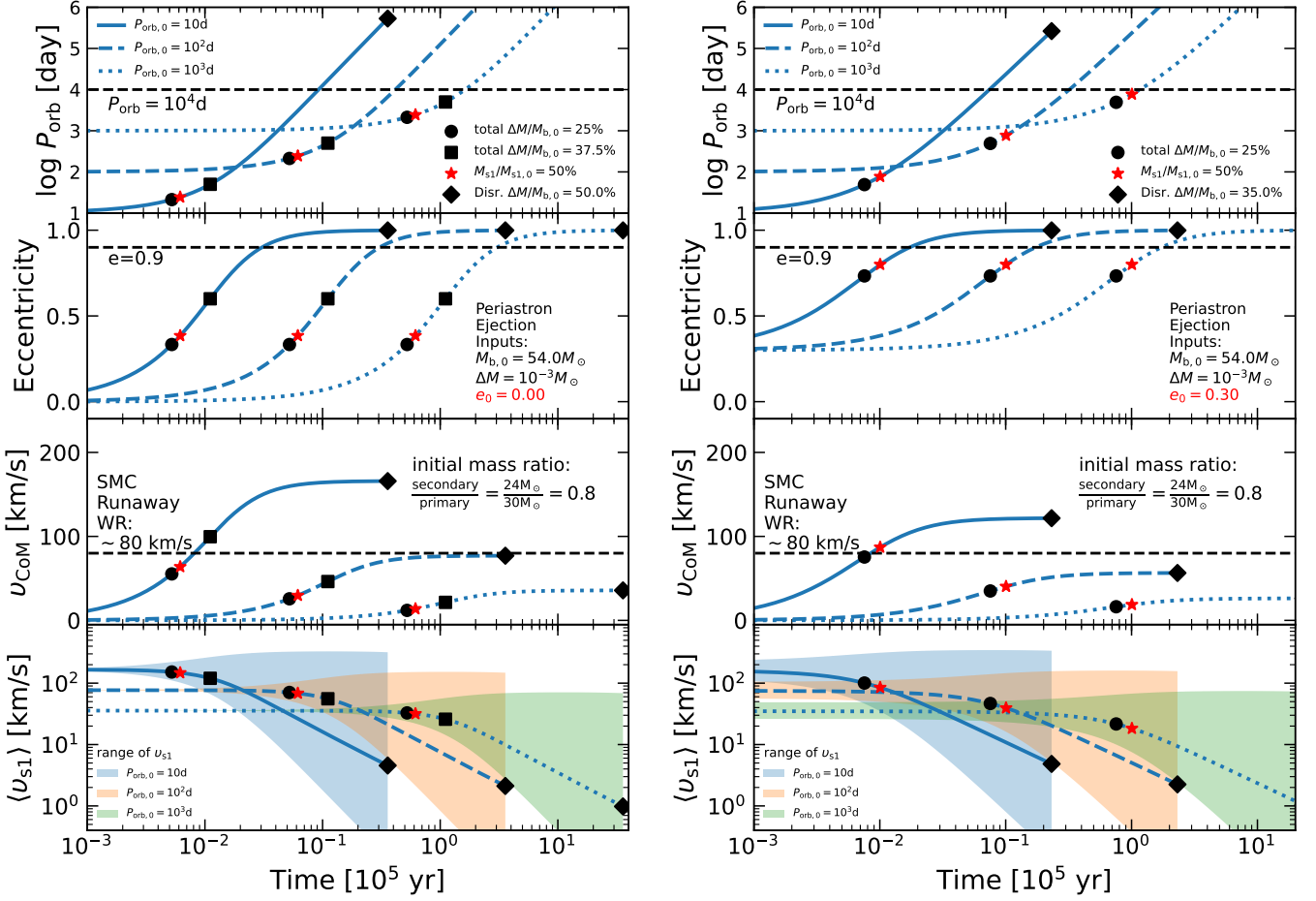


Fig. 3. Example models using the mass-ejection-driven orbital evolution, assuming that the primary star ejects a mass of $10^{-3} M_{\odot}$ during each periastron passage. The two columns correspond to two initial eccentricities, 0.0 (left) and 0.3 (right). From top to bottom, the panels present the evolution of orbital period, eccentricity, the velocity of the centre of mass, and the average orbital velocity of the mass-losing star. Each panel contains three curves, computed with different initial orbital periods, 10 d (solid line), 100 d (dashed line), and 1000 d (dotted line). The markers correspond to ejected masses of $25\% M_{b,0}$ (circle), $37.5\% M_{\odot}$ (square), and ΔM_{dis} (Eq. 30; diamond). In the $\langle v_{s1} \rangle$ panel, we used coloured regions to indicate the ranges of the orbital velocities of the mass-losing stars of different initial orbital periods (blue: 10 d; brown: 10^2 d; green: 10^3 d), where the upper and lower limits are determined by the velocities at periastron (Eq. 19) and apastron (Eq. 20). The red star means that the mass-losing star ejects half of its initial mass. The dashed lines mark $P_{\text{orb}} = 10^4$ d (assumed detection limit), $e = 0.9$ (the measured eccentricity of WR 140; Thomas et al. 2021), and $v_{\text{CoM}} = 80 \text{ km s}^{-1}$ (the observed peculiar velocities of SMC AB1 and AB11; Schootemeijer et al. 2024).

to infer the pre-mass-ejection properties of observed wide and eccentric WR+O binaries. We rewrote Eqs. (42)-(45) as

$$\frac{M_{\text{H-env}}}{M_{b,0}} = \frac{e_{\text{obs}} - e_0}{1 + e_{\text{obs}}}, \quad (59)$$

$$M_{s1,0} = \frac{M_{b,\text{obs}}}{1 - (M_{\text{H-env}}/M_{b,0})} - M_{\text{O}}, \quad (60)$$

$$P_{\text{orb},0}^2 = P_{\text{orb,obs}}^2 \frac{[(1 - e_0) - 2(M_{\text{H-env}}/M_{b,0})]^3}{[1 - (M_{\text{H-env}}/M_{b,0})]^2 (1 - e_0)^3}, \quad (61)$$

$$v_{\text{CoM,obs}} = \frac{M_{\text{H-env}} M_{\text{O}}}{M_{b,0} (M_{b,0} - M_{\text{H-env}})} v_{\text{per},0}, \quad (62)$$

where the subscript "0" indicates the value before the onset of the mass-ejection-driven orbital evolution, the subscript "obs" corresponds to the observed parameter of WR+O binaries, $M_{\text{H-env}}$ is the mass of the hydrogen-rich envelope of the WR progenitor, and M_{O} is the mass of the O star companion. With these equations, the pre-mass-ejection properties can be solved by varying the pre-mass-ejection eccentricity, e_0 , as a free parameter.

We used the above equations to infer the properties of the progenitor of WR 140, whose observed parameters are summarised in Tab. 1. Our results are presented in Fig. 4, where e_0 is treated as a free parameter, and we infer the other pre-mass-ejection parameters and predict the current space velocity of WR 140, $v_{\text{CoM,obs}}$. During the mass-ejection-driven orbital evolution, the mass of the O star companion was expected to remain unchanged. Hence, physical solutions should meet $M_{s1,0} \geq M_{\text{O}}$, which corresponds to the parameter space with $e_0 \leq 0.284$. The mass of the WR progenitor is limited to $30\text{--}45 M_{\odot}$, which is consistent with the value inferred by using the BPASS model (Thomas et al. 2021) and the MESA models computed with Galactic metallicity by Jin et al. (2024) and Jin et al. (2025)⁵. We describe the method of fitting with the MESA models in Appendix C. While the current orbital period of WR 140 is about 2895 d, we expect the progenitor system to have an orbital period below ~ 100 d. In addition, we predict the current space velocity of WR 140 to be about $50\text{--}75 \text{ km s}^{-1}$, which does not

⁵ The model data is available: <https://www.mpa.mpa-garching.mpg.de/stellgrid/>.

Table 1. Observed properties of WR 140.

WR140		Refs
O-type star mass (M_{O})	$29.27 M_{\odot}$	(1)
WR companion (M_{WR})	$10.31 M_{\odot}$	(1)
orbital period ($P_{\text{orb,obs}}$)	2895 d	(1)
eccentricity (e_{obs})	0.8993	(1)
proper motion	$\sim 34 \pm 2 \text{ km s}^{-1}$	(2)

Notes. (1) Thomas et al. (2021); (2) Dzib & Rodríguez (2009).

Table 2. Definitions of our population synthesis models.

	Simulation1	High- M_{crit}	High- P_{crit}	Flat- f_e
$M_{\text{crit}} [M_{\odot}]$	30	40	=	=
$P_{\text{crit}} [\text{d}]$	40	=	60	=
η	0.5	=	=	0

Notes. "=" means the same value as that in Simulation1.

contradict the observed proper motion of WR 140 ($\sim 34 \text{ km s}^{-1}$; Dzib & Rodríguez 2009). Therefore, our mass-ejection-driven orbital evolution can self-consistently explain the formation of WR 140-like systems.

3.3. Population synthesis predictions

3.3.1. Predictions with fixed initial eccentricities

To better interpret our population synthesis predictions by Simulation1, we present the predictions with fixed initial eccentricities (0.4 and 0.6) and the values for M_{crit} and P_{crit} in the first place. Predictions with other initial eccentricities are provided in Appendix D.

Without the mass-ejection-driven orbital evolution, Simulation2 predicts 11 WR+O binaries in the SMC, whose orbital period distribution peaks at $\sim 10 \text{ d}$ and decays to $\sim 1000 \text{ d}$, of which 4.3 WR+O binaries are predicted to have orbital periods below the observed longest orbital period, 20 d, which is consistent with the observed number of close SMC WR+O binaries (4; Shenar et al. 2016, 2018; Schootemeijer & Langer 2018; Schootemeijer et al. 2024). According to our criterion of entering the mass-ejection-driven orbital evolution, 5.3 WR+O binaries are formed from the mass-transfer-driven orbital evolution (hereafter mass-transfer WR+O binaries), whose number rapidly drops towards the long-period regime ($\sim 100 \text{ d}$), and 5.7 WR stars are formed from the mass-ejection-driven orbital evolution, of which the fractions that remain bound (hereafter mass-ejection WR+O binaries) and get disrupted (runaway WR stars) sensitively depend on the assumed initial eccentricities.

Figure 5 presents the result with $e_0 = 0.4$, where 3.7 mass-ejection WR+O binaries are expected, whose orbital periods are widely distributed from about 300 d to 10^5 d with a peak at around 3000 d. The number drops towards the long-period regime is caused by binary disruption and the effect of the initial orbital period function, and the number drop towards the short-period regime reflects the lower chance of entering the mass-ejection-driven orbital evolution. The mass-transfer WR+O binaries have a maximal orbital period about 100 d, which can reach up to 1000 d for a higher M_{crit} (cf., Sect. 3.3.3 and App. E).

The 2D distributions show that the predicted P_{orb} , v_{COM} , and $\langle v_{\text{s1}} \rangle$ are correlated with eccentricity, which can be explained

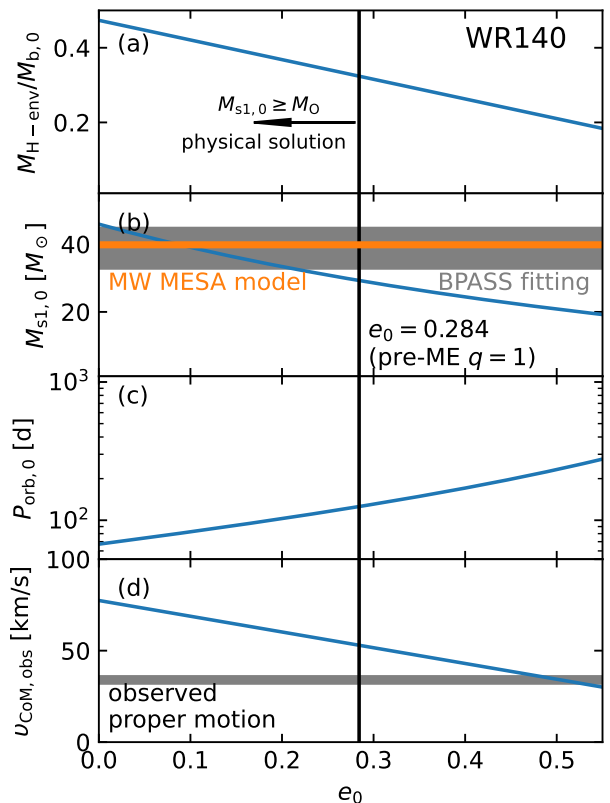


Fig. 4. Inferred properties of the progenitor of WR 140 as a function of the pre-mass-ejection eccentricity. Panel (a) presents the inferred mass ejection fraction, which is the mass of the hydrogen-rich envelope of the primary star divided by the pre-mass-ejection binary mass. Panel (b) presents the inferred pre-mass-ejection mass of the WR progenitor, using the BPASS model (Thomas et al. 2021) and the MESA model (Jin et al. 2024, 2025), respectively, for comparison. Panel (c) presents the pre-mass-ejection orbital period. Panel (d) presents the predicted current velocity of the centre of mass, where the grey region indicates the observed proper motion of WR 140 (Dzib & Rodríguez 2009).

by Eqs. (46)-(48). The majority of these long-period (10^3 - 10^4 d) binaries are near disruption, featuring eccentricities of 0.8-1.0. The corresponding velocities of the centre of mass are about 20-60 km s^{-1} . Since high-eccentricity systems tend to have wide orbits, more eccentric binaries are associated with lower average orbital velocities for the WR stars, 0-40 km s^{-1} .

The distribution of the masses of the WR stars in these mass-ejection WR+O binaries peaks at about $15 M_{\odot}$ and decays towards the high-mass end due to the effect of the initial mass function. The model grid in Xu et al. (2025b) is not linearly spaced in initial primary mass, and this grid effect is likely responsible for the flat feature in $[20 M_{\odot}, 30 M_{\odot}]$. The mass ratio (q_{WR} : WR star/OB star) distribution peaks at about 0.7. Here q_{WR} can be estimated by

$$q_{\text{WR}} = \frac{M_{\text{WR}}}{M_{\text{OB}}} = \frac{M_{\text{WR}}/M_{1,i}}{M_{\text{OB}}/M_{1,i}} \approx \frac{0.5}{q_i}, \quad (63)$$

where M_{OB} is the mass of the OB star companion. Therefore, the peak of the q_{WR} distribution at 0.7 also corresponds to a q_i of about 0.7. Binaries with $q_i > 0.7$ are lacking because most of them merge in Xu et al. (2025b) due to the occurrence of inverse mass transfer with a post-MS mass gainer. The number drops towards the high- q_{WR} regime because a high q_{WR} is associated

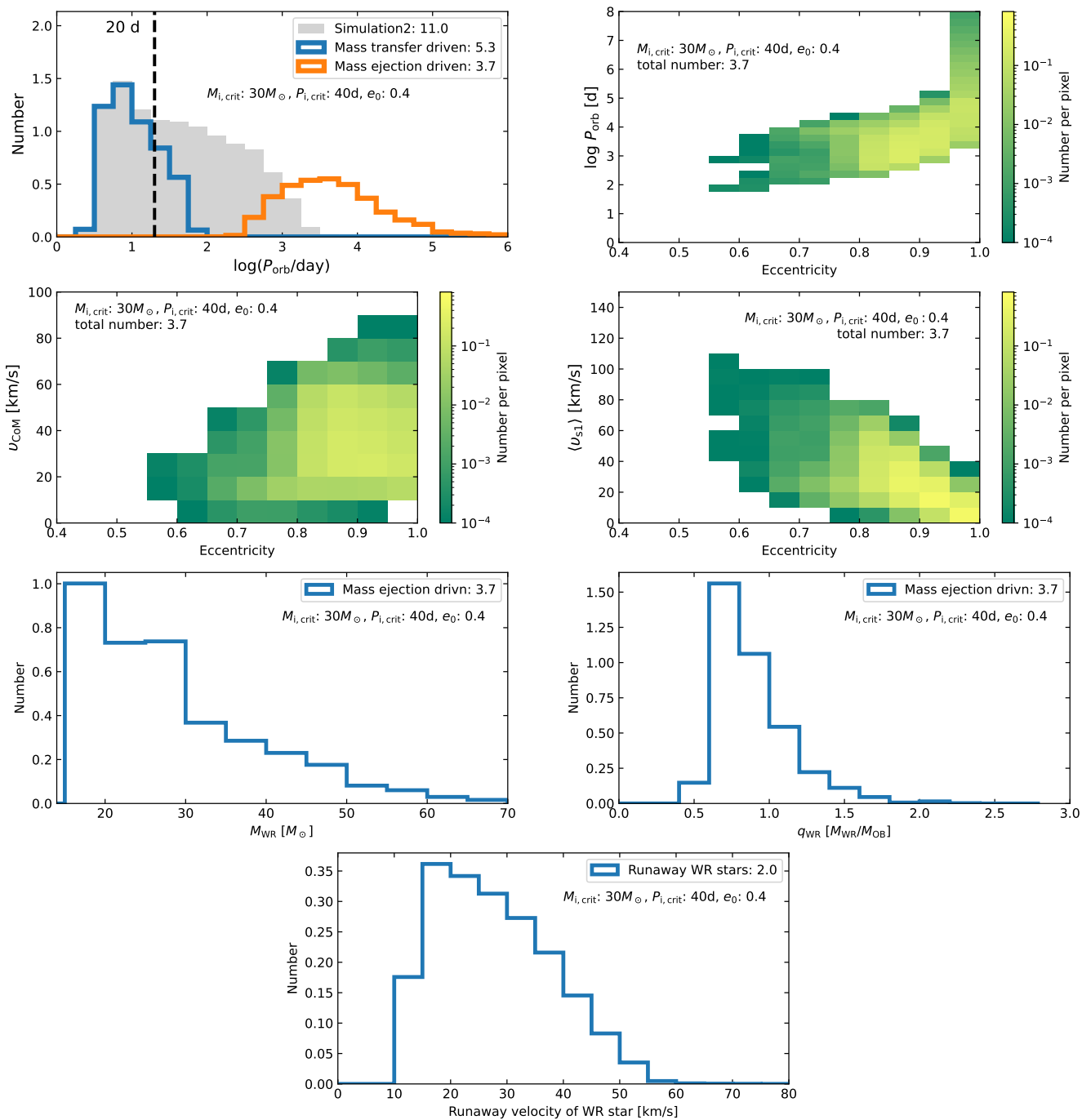


Fig. 5. Population synthesis predictions with a fixed initial eccentricity, 0.4. The upper-left panel presents the predicted orbital period distribution, where the systems formed through the mass-transfer- and mass-ejection-driven orbital evolution are plotted in blue and orange, respectively, and the text indicates the predicted numbers. The vertical dashed line marks the longest orbital period (20 d) of the observed WR+O binaries in the SMC. The prediction by Simulation2, which is the fiducial model in Xu et al. (2025b) but with a higher star formation rate, is plotted in grey for comparison. The 2D distributions are the mass-ejection WR+O population on the eccentricity- $\log P_{\text{orb}}$ (upper-right), $-v_{\text{CoM}}$ (middle-left) and $\langle v_{s1} \rangle$ (middle-right) planes, where the predicted number in each pixel is colour-coded. The third row presents the predicted distributions of WR star masses (M_{WR}) and mass ratios (WR star/O star) of the mass-ejection WR+O binaries. The bottom panel presents the predicted space velocities of the runaway WR stars.

with a low q_i , where Xu et al. (2025b) expect a large merger fraction (see also Langer et al. 2020; Henneco et al. 2024). These merging binaries in Xu et al. (2025b) can avoid merging if the primary stars evolve through an LBV stage, which our population synthesis cannot assess, as our calculation is limited by the model data in Xu et al. (2025b).

There are about 2.0 runaway WR stars with $e_0 = 0.4$, most of which have runaway velocities of $\sim 20 \text{ km s}^{-1}$. The runaway velocities are approximated by the velocities of the centre of mass at disruption (Eq. 52), which is proportional to $P_{\text{orb},0}^{-1/3}$ (Eq. 10). Hence the number drop towards the high-velocity regime is due to the effect of the initial orbital period function.

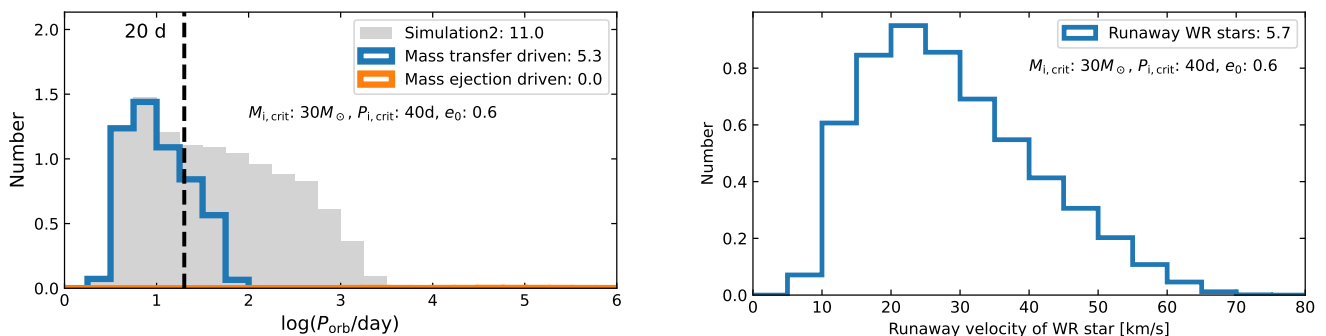


Fig. 6. Population synthesis predictions with a fixed initial eccentricity, 0.6. The left panel presents the predicted orbital period distribution, and the right panel presents the predicted space velocities of the runaway WR stars. The colours have the same meaning as in the upper-left and bottom panels of Fig. 5.

The lowest eccentricity we predict is about 0.55 with $e_0 = 0.4$, corresponding to a mass ejection fraction of about 10%. We note that the predicted population with eccentricities close to the assumed initial eccentricity should be treated with caution, as we notice that Xu et al. (2025b) misclassified a few mass-transferring systems as WR+O binaries, which only takes a small fraction of the predicted population by Xu et al. (2025b), and should not affect the main conclusion of this work.

By taking $e_0 = 0.6$, all binaries entering the mass-ejection-driven orbital evolution get disrupted (Fig. 6) because of a lower ΔM_{dis} , which can be expressed as a function of $M_{1,i}$ and q_i ,

$$\frac{\Delta M_{\text{dis}}}{M_{1,i}} = \frac{1}{2}(1 + q_i)(1 - e_0). \quad (64)$$

The binaries with higher q_i are harder to disrupt. With $q_i = 1$ and $e_0 = 0.6$, we have $\Delta M_{\text{dis}}/M_{1,i} = 0.4$. Most of the primary stars lose about half of their initial masses during the mass-ejection-driven orbital evolution (i.e., $M_{\text{H-env}}/M_{1,i} = 0.5$), which exceeds the amount required for disruption. The space velocities of runaway WR stars have a similar distribution as the $e_0 = 0.4$ case.

3.3.2. Predictions with the initial eccentricity function

The properties of the synthetic population by Simulation1 are presented in Fig. 7, which shows similar features as the predicted population with $e_0 = 0.4$ (Fig. 5). With $\eta = 0.5$, about 63% of pre-mass-ejection binaries have eccentricities below 0.4 according to Eq. (57). Consequently, the predicted orbital periods of the mass-ejection WR+O binaries, peaking at around 562 d (2.75 in log), are generally shorter than in the $e_0 = 0.4$ case (Fig. 5), and the expected average orbital velocities ($\langle v_{s1} \rangle$: 20–100 km s⁻¹), higher than the $e_0 = 0.4$ case. For the same reason, the predicted eccentricities are widely distributed from about 0.4 to 1. The predicted distributions of M_{WR} and q_{WR} show the same peak value as the $e_0 = 0.4$ case, which are $\sim 15 M_{\odot}$ and ~ 0.7 respectively. The predicted v_{CoM} covers the peculiar velocities of SMC AB1 and SMC AB11 (~ 80 km s⁻¹; Schootemeijer et al. 2024), but the high-velocity population only takes a small fraction of the whole population. In addition, we predict 1.9 runaway WR stars, whose runaway velocity distribution peaks at 10–20 km s⁻¹ and decays to about 60 km s⁻¹.

3.3.3. Parameter study

By varying the values of M_{crit} , P_{crit} , and η , we constructed three population synthesis models, besides Simulation1, whose properties are summarised in Tab. 2. Table 3 presents the predictions

by different population synthesis models. We provide the predicted distribution functions in Appendix E. The main differences lie in the predicted numbers and predicted orbital period distributions.

A higher M_{crit} can largely reduce the predicted number of mass-ejection WR+O binaries due to the effect of the initial mass function. The High- M_{crit} model predicts 8.1 mass-transfer WR+O binaries (Simulation1: 5.3), of which a considerable fraction have orbital periods above 20 d with a maximal orbital period of 1000 d. This long-period tail does not show up in Simulation1 because all WR star progenitors in initially wide binaries have the LBV phase with $M_{\text{crit}} = 30 M_{\odot}$. There are 2.9 WR star systems formed through the mass-ejection-driven orbital evolution, of which 2.0 remain bound, and 0.9 get disrupted, and the peak orbital period of the mass-ejection WR+O binaries is similar to that predicted by Simulation1.

Changing P_{crit} from 40 d to 60 d does not significantly alter the predicted numbers. The High- P_{crit} model predicts 6.1 mass-transfer WR+O binaries, 3.2 mass-ejection WR+O binaries, and 1.7 runaway WR star. These predicted numbers are similar to those in Simulation1. As expected, with a higher P_{crit} , the maximal orbital period of the mass-transfer WR+O binaries reaches 100 d (fiducial: 56 d), and the peak orbital period of the mass-ejection WR+O binaries also becomes slightly longer (from 562 d to 750 d).

A flat initial eccentricity distribution leads to fewer low-eccentricity pre-mass-ejection binaries than in Simulation1. For example, 40% binaries have initial eccentricities below 0.4 in the Flat- f_e model, which is 63% in Simulation1. Hence, more runaway WR stars can be expected (Flat- f_e : 3.2; Simulation1: 1.9). Since binary disruption becomes generally easier than in Simulation1, the peak orbital period of the mass-ejection WR+O binaries is shifted to 1000 d (Flat- f_e) from 562 d (Simulation1).

3.4. Second-born Wolf-Rayet stars

A detailed population synthesis calculation which includes WR stars formed by the initial secondary stars (second-born WR stars) is beyond the scope of this paper. In this subsection, we used simplified assumptions to estimate the population of the second-born WR stars based on the synthetic population of the first-born WR stars in Simulation1.

All WR stars are assumed to be BH progenitors, and we take the mass of the WR star at core helium depletion as the mass of the resulting BH. Consequently, the resulting BH+O binaries have the same orbital properties as their direct progenitors (i.e., the WR+O binaries). Consistent with Simulation1, we apply the

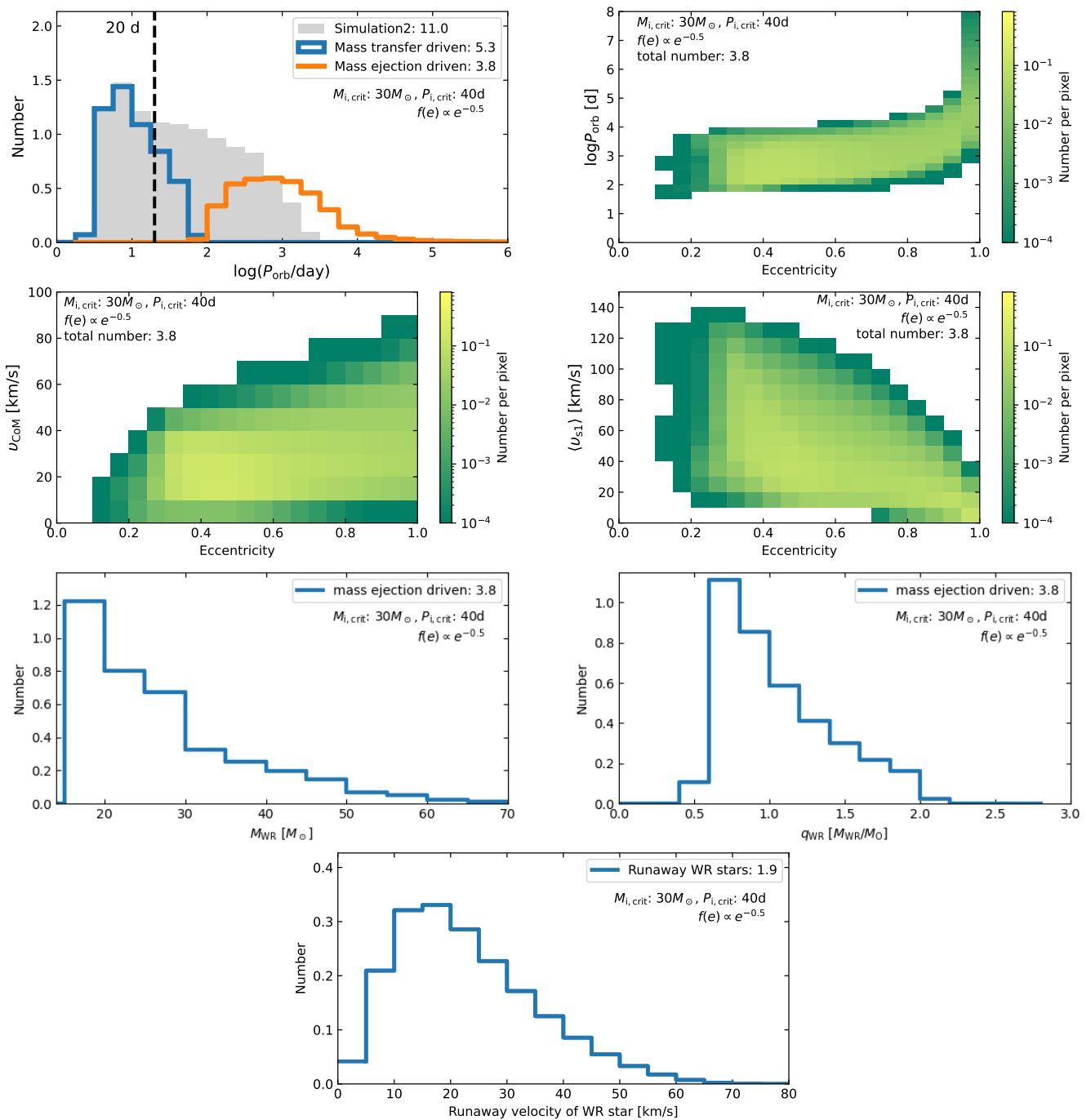


Fig. 7. Population synthesis predictions with the initial eccentricity function in Sana et al. (2012) (i.e., Simulation1 in Tab. 2). The colours have the same meanings as Fig. 5.

criterion described in Sect. 3.3 with $(M_{\text{crit}}, P_{\text{crit}}) = (30 M_{\odot}, 40 \text{ d})$ to determine whether the orbital evolution of a BH+O binary model is also driven by LBV mass ejections. If so, we assume that the O star loses half of its mass in the process. Xu et al. (2025b) define a WR star as a core helium-burning star with an luminosity above $10^{5.6} L_{\odot}$, which corresponds to a minimum WR star mass of about $14 M_{\odot}$ and a zero-age main-sequence mass of about $30 M_{\odot}$ ⁶. Hence, we only considered the evolution of BH+O binaries with O star companions more massive than

⁶ Mass transfer during the main-sequence phase of the donor star produces lighter helium stars (Sen et al. 2022; Schürmann et al. 2024), whose parameter space however is negligible in this study.

$30 M_{\odot}$. To estimate the number of the WR stars, we calculated their statistical weight (Eq. 58) with a typical lifetime, 0.4 Myr, for all second-born WR stars.

Our results are summarised in Tab. 4. They suggest that second-born WR stars may comprise about 1/3rd of the WR star population. Their number is similar (within a factor 2) to the number of WR+OB systems because of their similar lifetimes, which are the lifetime of the WR stars (van den Heuvel et al. (2017), and Chapter 3 in Xu (2024)). While we find that about two third of the second-born WR stars would be born from classical mass transfer (to their BH companions), about one third is massive enough (cf., the q_{WR} distribution in Fig. 7) to evolve through the LBV mass ejection channel. In those, the eccentric-

Table 3. Prediction from our different population synthesis models.

	Predicted numbers of WR star systems			Predicted orbital period distributions			
	mass transfer	mass ejection	runaway	$P_{\text{MT,max}}$ [d]	(log)	$P_{\text{ME,peak}}$ [d]	(log)
Simulation1	5.3	3.8	1.9	56	(1.75)	562^{+438}_{-246}	$(2.75^{+0.25}_{-0.25})$
High- M_{crit}	8.1	2.0	0.9	1000	(3.0)	422^{+578}_{-244}	$(2.625^{+0.375}_{-0.375})$
High- P_{crit}	6.1	3.2	1.7	100	(2.0)	750^{+1028}_{-434}	$(2.875^{+0.375}_{-0.375})$
Flat- f_e	5.3	2.5	3.2	56	(1.75)	1000^{+778}_{-438}	$(3^{+0.25}_{-0.25})$

Notes. See Tab. 2 for the definitions of the population synthesis models. The 2nd–4th columns are the predicted numbers of mass-transfer WR+O binaries, mass-ejection WR+O binaries, and runaway WR stars, respectively. The 5th–8th columns describe the predicted orbital period distributions of mass-ejection/mass-transfer WR+O binaries by using two parameters, which are the maximal orbital period of mass-transfer WR+O binaries, $P_{\text{MT,max}}$, and the peak orbital period of the distributions of mass-ejection WR+O binaries, $P_{\text{ME,peak}}$ (see Appendix E for the predicted distribution functions).

Table 4. Predicted fractions (number in each subclass divided by the total number of WR stars) of first- and second-born WR stars in the SMC.

First-born WR star: 67.2%	
mass-transfer WR+O	32.4%
mass-ejection WR+O	23.2%
runaway WR	11.6%
Second-born WR star: 32.8%	
mass-transfer BH+WR	22.6%
mass-ejection BH+WR	4.8%
runaway WR	5.4%

Notes. The synthetic population of the first-born WR stars is taken from Simulation1, and the population of the second-born WR stars is derived from it with simplified assumptions (see Sect. 3.4).

ities are already large due to the first LBV driven interaction phase, such that their disruption rate is higher ($\sim 50\%$) than that of the first LBV driven phase ($\sim 33\%$).

In our population synthesis calculation, we normalised the predicted number of the first-born WR stars to the observed number (11), which corresponds to a constant star formation rate of $0.0821 M_{\odot} \text{ yr}^{-1}$. After including the second-born WR stars, we find that the observed number can be reproduced by a star formation rate of $0.055 M_{\odot} \text{ yr}^{-1}$, which is well consistent with the value, $0.05 M_{\odot}$, adopted in Xu et al. (2025b).

4. Discussion

4.1. The number of long-period Wolf-Rayet star binaries

Our population synthesis predictions show that our mass ejection scenario transforms the period- and eccentricity distributions of the long-period WR binary population. Our Simulation1 predicts 5.3 close WR+O binaries (4 observed in the SMC; Shenar et al. 2016, 2018; Schootemeijer & Langer 2018; Schootemeijer et al. 2024), 3.8 wide WR+O binaries, most of which may not be ruled out by previous radial-velocity searches and exhibit measurable space velocities, and 1.9 runaway WR stars (7 single WR stars observed in the SMC, including 2 runaway stars; Schootemeijer et al. 2024). The space velocities of the observed runaway WR stars imply that their progenitors may have had relatively high eccentricities and short orbital periods, or the past mass ejections may have generated additional momentum kicks. For the predicted wide WR+O binaries, it might be difficult to detect their binarity, but not impossible. If such systems were

truly missing in the SMC, perhaps wide SMC O star binaries are more eccentric than we assumed, and more often disrupted. For Simulation2, the synthetic WR+O binaries contains a large fraction of binaries with orbital period between 20 d and 1 yr, whose binarity would be identified by Schootemeijer et al. (2024) if they existed. Besides potential massive companions suggested by our results, companions below $\sim 5 M_{\odot}$ to these apparently single SMC WR stars are also not excluded (Olejak et al. 2025). In addition, Schootemeijer et al. (2024) also report the absence of the He I 4471 Å line and no significant correlation between successive observations and the radial-velocity differences between them, whose implications for the binarity of the SMC WR stars are beyond the scope of this work.

We note that the above numbers focus on the LBV stage of the primary stars in wide O star binaries. As discussed in Sect. 3.4, the secondary stars might also evolve through an LBV stage, triggering a second mass-ejection-driven orbital evolution and forming second-born WR stars, whose number might be about half that of the first-born WR stars. Some apparently single SMC WR stars may also originate from the self-stripping of single stars (Shenar et al. 2020). Assuming 70% of the SMC O stars are in binary systems, and half of the single O stars are massive enough to reach their Eddington limit and self-strip, about 15% of the SMC WR stars might be formed through self-stripping. Therefore, our population synthesis calculations might only cover about half of the SMC WR star population.

Our mass-ejection-driven orbital evolution model predicts that the binary fractions roughly remain unchanged from O stars to LBVs, but decrease significantly for WR stars, which is consistent with current observations. The binary fractions of Galactic O stars and LBVs are observed to be about 70% (Sana et al. 2012) and $62^{+38}_{-24}\%$ (bias corrected binary fraction; Mahy et al. 2022), but the binary fraction of WR stars significantly drops to about 36% (4/11) according to the SMC sample, or about 40% according to the LMC sample (107 WR stars, of which 17 confirmed and 22 candidate binary systems; Hainich et al. 2014), suggesting that some of the single WR stars may be WR 140-like systems or runaway stars.

4.2. Implication for the orbital period distributions of Galactic WNE and WC star binaries

Carbon-rich WR stars are suggested to evolve from early-type nitrogen-rich WR (WNE) stars through wind mass loss (Langer 1987, 2012). As a consequence, a WNE binary evolves into a WC binary, with its orbital evolution driven by wind mass loss. However, the observed orbital period distributions of Galactic

WN and WC binaries seem inconsistent with the above theoretical expectation, peaking at 1–10 d for WN binaries, but at about 5000 d for WC binaries (Dsilva et al. 2023). The limited sample size might cause this potential tension (Deshmukh et al. 2024). More observational data is required to verify whether the orbital period distributions of WNE and WC binaries are different or not.

If the orbital period distributions of WNE and WC binaries are truly in tension with each other, the mass-ejection-driven orbital evolution proposed in this work may offer a plausible explanation, given that we have shown one of these long-period WC binaries, WR 140, could result from such evolution (cf., Sect. 3.2). More massive helium stars spend more of their lifetime as WC stars (Aguilera-Dena et al. 2022), and their progenitor stars have more chance to reach the Eddington limit, triggering the LBV mass ejection and resulting in the long-period WC binaries. The observed WNE binaries are more likely to originate from less massive systems, since less massive helium stars remain as WN stars during the lifetime (Aguilera-Dena et al. 2022), and they are preferred by the initial mass function. Most of the progenitor stars are not massive enough to reach the Eddington limit, and hence mass transfer drives the orbital evolution, resulting in an orbital period distribution for WN binaries similar to O star binaries, as found by Dsilva et al. (2023).

4.3. Implication for merging binary black holes

As indicated in Fig. 1, the lack of long-period WR binaries includes those expected to enter common envelope evolution, which may have strong implications for the formation of merging BBHs. If the O stars in wide binaries disappear because they merge with their companions during the first mass transfer phase, they cannot form BBHs.

If the mass-ejection-driven orbital evolution is responsible for the lack of observed long-period WR binaries, merging BBHs can hardly be formed in wide binaries either. Figure 8 shows a schematic plot of the evolution of initially wide O star binaries with the mass-ejection-driven orbital evolution. It suggests that the long-period WR binaries appear as single stars, or that most of wide O star binaries are disrupted by the LBV mass ejection. Then, if the binary can survive the LBV stage, the existence of long-period and eccentric BH+O binaries can be expected, if the WR stars can successfully collapse into BHs. Different from the prediction by Xu et al. (2025b) that most of the OB star companions to BHs are fast-rotating, we expect the O stars to remain rotating slowly. Then the expansion of the companion star triggers the mass transfer in eccentric binaries (Sepinsky et al. 2007, 2009; Rocha et al. 2025; Parkosidis et al. 2025a) or a second episode of mass-ejection-driven orbital evolution. Orbital widening and eccentricity enhancement take place in both cases, resulting in long-period and eccentric WR+BH binaries or binary disruption, which can hardly form merging BBHs. The formation of merging BBHs is possible only if the tide is strong enough to circularise the orbit, and the companion star can avoid the LBV phase. Then the future evolution of the system can be described by the mass transfer through Roche-lobe overflow, where merging BBHs are formed through either the CEE channel (Belczynski et al. 2016) or the stable mass transfer channel (Marchant et al. 2021; Klencki et al. 2025; Xu et al. 2025a; Briel et al. 2026). In addition, for eccentric low-mass systems, a similar mechanism, *gazing envelope evolution*, has been proposed by Kashi & Soker (2018).

4.4. Implication for Gaia black hole systems

The recently detected Gaia BH systems contain a low-mass star orbiting a massive BH in a wide and eccentric orbit (see Tab. 5). It has been suggested that they have been formed by dynamical interaction in star clusters (Rastello et al. 2023) or in triple star systems (Naoz et al. 2025). Evolutionary channels in isolated binary systems have also been identified, with some scenarios involving BH kicks (Kotko et al. 2024), and others relying on the avoidance of mass transfer from the BH progenitors to the low-mass companions (Gilkis & Mazeh 2024; Olejak et al. 2025). The latter scenarios usually have difficulties producing the eccentricities of Gaia BH1 and BH2, while Gaia BH3 can be explained by wide non-interacting binaries (Iorio et al. 2024). The mass-ejection-driven orbital evolution might provide a mechanism to pump eccentricities in Gaia BH progenitor systems. In the following, we investigate whether our model can provide a formation scenario for the systems Gaia BH1 and BH2, to estimate the properties of their progenitor systems.

Different to the SMC models, stellar wind mass loss may be important in Galactic massive binaries. Assuming that the Gaia BHs formed through direct collapse, the initial mass of the progenitor WR star can be estimated by $f_{\text{WR,wind}} M_{\text{BH}}$, where M_{BH} is the BH mass, and the $f_{\text{WR,wind}}$ factor captures the effect of WR star winds. We adopted $f_{\text{WR,wind}} = 2$, implying that a $20 M_{\odot}$ WR star would lose half of its mass through winds, and produces a $10 M_{\odot}$ BH. Since the Gaia BHs and their progenitor stars are more massive than their low-mass companions, the binary masses can be approximated by the primary masses⁷. Then, according to Eqs. (59) and (60), the ejected mass required to produce the observed eccentricities, $M_{\text{ej,per}}$, can be estimated by

$$M_{\text{ej,per}} \approx f_{\text{WR,wind}} \left[\frac{M_{\text{BH}}}{1 - (e_{\text{obs}} - e_0)/(1 + e_{\text{obs}})} - M_{\text{BH}} \right]. \quad (65)$$

For $e_{\text{obs}} = 0.5$, $e_0 = 0$ (i.e., a circular pre-mass-ejection orbit), and $M_{\text{BH}} = 10 M_{\odot}$, our model requires the progenitors of Gaia BH1 and BH2 to eject $10 M_{\odot}$ during the LBV phase. Based on the MESA models computed by Jin et al. (2025), this could be achieved from a star with an initial mass of about $50 M_{\odot}$, which has lost about $20 M_{\odot}$ through a wind during its main-sequence evolution, before entering its LBV phase with a $10 M_{\odot}$ hydrogen-rich envelope.

The required pre-LBV orbital separation can be estimated by using Eq. (61) with Kepler’s third law, which is

$$\frac{a_i^3}{a_f^3} = \frac{M_{\text{ej,per}} + f_{\text{WR,wind}} M_{\text{BH}} [(1 - e_0) - 2(M_{\text{H-env}}/M_{\text{b},0})]^3}{f_{\text{WR,wind}} M_{\text{BH}} [1 - (M_{\text{H-env}}/M_{\text{b},0})]^2 (1 - e_0)^3}, \quad (66)$$

where a_i and a_f are the semi-major axes before and immediately after the LBV phase, respectively. Assuming again $e_0 = 0$, a_i is equal to the pre-LBV orbital separation, and we have $M_{\text{H-env}}/M_{\text{b},0} \approx 1/3$ for Gaia BH1 and BH2, which leads to $a_i/a_f \approx 1/2$. After the LBV phase, the orbit keeps widening due to the WR winds, while the eccentricity obtained during the LBV phase is preserved. For isotropic mass loss (Eq. 16.20 in Tauris & van den Heuvel 2006), we find that the WR winds widen the orbit by a factor of two, i.e., $a_f \approx a_{\text{obs}}/2$, where a_{obs} denotes the currently observed semi-major axis. Therefore, the pre-LBV orbital separation is about 1/4th of the observed semi-major axis, resulting in $80 R_{\odot}$ and $280 R_{\odot}$ for the progenitors of

⁷ $M_{\text{b},0} \approx M_{\text{s},0}$ in Eq. (59), $M_{\text{b,obs}} \approx M_{\text{BH}}$ in Eq. (60), and the companion mass term, M_0 , in Eq. (60) can also be ignored.

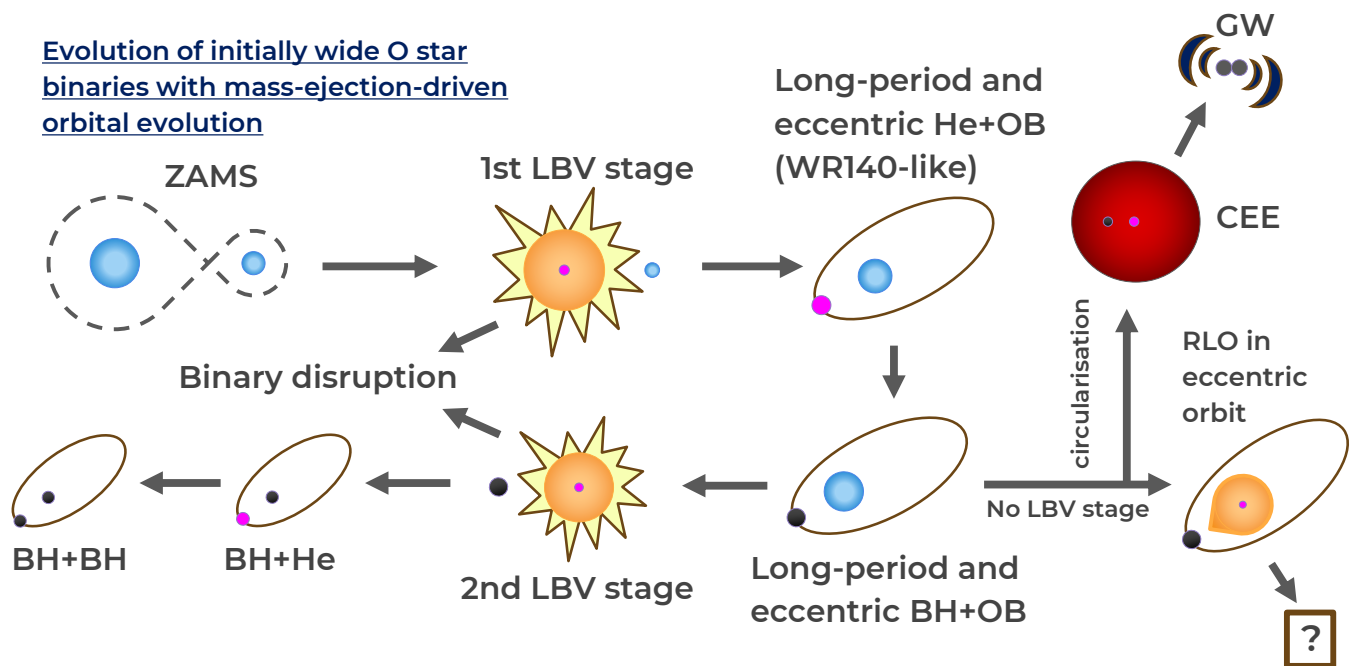


Fig. 8. Schematic evolutionary sequence for initially wide O star binaries with the mass-ejection-driven orbital evolution. The abbreviations have the same meaning as Fig. 1.

Table 5. Properties of Gaia black hole systems

System	Gaia BH1	Gaia BH2	Gaia BH3
P_{orb} [d]	185.6	1277	4234 (11.6 yr)
Eccentricity	0.45	0.52	0.73
BH mass [M_{\odot}]	9.62 ± 0.18	8.9 ± 0.3	32.7 ± 0.8
Companion			
- mass [M_{\odot}]	0.93 ± 0.05	1.07 ± 0.19	0.76 ± 0.05
- metallicity	solar-like	slightly low	low
[Fe/H]	-0.2	-0.22	-2.56
Reference	(1)	(2)	(3)

Notes. (1) El-Badry et al. (2023b); (2) El-Badry et al. (2023a); (3) Gaia Collaboration et al. (2024).

Gaia BH1 and Gaia BH2. The sizes of LBVs range from tens to hundreds of solar radii. E.g., AG Carinae exhibits a radius changing from $\sim 80 R_{\odot}$ to above $160 R_{\odot}$ (Groh et al. 2011). The estimated orbital separations before and after the LBV stage of our models are well compatible to these numbers.

It is beyond our scope to produce best-fit progenitor models for the Gaia BH systems. However, the example case explored above shows that our scenario of LBV-driven mass ejections may offer a viable explanation for the origin of Gaia BH1 and Gaia BH2.

4.5. Trigger mechanisms of mass ejection at periastron

Observationally, LBVs display two types of eruptions, S Doradus eruptions (Wolf 1989) and giant eruptions, such as observed in η Carinae (Smith et al. 2003) and P Cygni (Smith & Hartigan 2006). While the mechanism of the giant eruptions remains unclear, the S Doradus eruptions likely occur in stars that reach or exceed their Eddington-limit, which leads to a loosely-bound inflated envelope of typically $10^{-3} M_{\odot}$

(Gräfener et al. 2012; Sanyal et al. 2015; Grassitelli et al. 2021; Cheng et al. 2024; Pauli et al. 2026). In this situation, small variations of the stellar wind mass-loss rate can induce strong structural changes of the inflated envelope, which may reproduce the observed S Doradus variability (Grassitelli et al. 2021). For this to occur, the mass of the stars needs to exceed $\sim 30 M_{\odot}$ in the Milky Way, and $\sim 40 M_{\odot}$ in the SMC (Sanyal et al. 2017).

When we envision a massive primary star to undergo envelope inflation prior to Roche lobe filling, the binary orbit will likely be eccentric. So far, the effect of envelope inflation in eccentric binaries has not been investigated. However, when the primary expands, it will encounter the situation of Roche-lobe filling at periastron passage. Since the inflated envelopes are radiation pressure dominated, they are only loosely bound to the star. Therefore, it may be plausible that such envelopes are simply kicked off when the primary moves through its periastron. If this happens, the inflated envelope will grow back and the primary finds itself in the same situation as before, except that over time the stellar mass is reduced and the Eddington factor increased, which makes the occurrence of the following mass ejections at periastron easier.

The current binary star, η Carinae, may give a potential counterpart of this situation (Hillier et al. 2001; Smith et al. 2018; Strawn et al. 2023), which shows series of brightening episodes (Smith & Frew 2011; Smith 2017a) and mass-loss enhancements (Corcoran et al. 2001) during periastron passages. Whereas not the whole hydrogen-rich envelope of the LBV primary stars is lost in this way, our model likely captures the main features of such events.

4.6. Apsidal Advance

Apsidal advance refers to the changing of orbital orientation within the orbital plane, which can happen if the mass ejection does not occur exactly at periastron or apastron (i.e., $\vec{v}_{\text{orb}} \cdot \vec{r} \neq 0$

in Eq. 32), or if a third body exists (von Zeipel 1910; Lidov 1962; Kozai 1962; Lei et al. 2018). In particular, a considerable fraction of massive stars are known to be in triple systems (Moe & Di Stefano 2017). We expect that apsidal advance can significantly reduce the velocity of the centre of mass but does not affect the evolution of other parameters. A detailed consideration of apsidal advance is beyond the scope of this work. In the following, we estimate its effect by assuming that the mass ejection occurs at periastron and that the periastron rotates at a constant angular velocity (ω_{ap} ; see Appendix F for details), which was taken to be

$$\omega_{\text{ap}} = \frac{2\pi}{10^4 P_{\text{orb},0}}. \quad (67)$$

We find that all the example models in Fig. 3 end up with v_{CoM} below 5 km s^{-1} due to apsidal advance (Fig. F.2). Therefore, our predicted space velocities should be treated as an upper limit.

5. Conclusion

A lack of observed long-period post-mass-transfer WR star binaries compared to predictions challenges our understanding of the evolution of initially wide O star binaries and has strong implications for the formation of merging BBHs. In this work, we explored the scenario that very massive wide O star binaries experience orbital evolution that is driven by LBV-type mass ejection occurring at periastron passages. We have derived the corresponding equations, presented a case study for the eccentric WR binary, WR 140, and performed population synthesis predictions for the WR stars in the SMC.

Different from the classical mass-transfer-driven orbital evolution usually adopted in current binary evolution models, the mass-ejection-driven orbital evolution increases orbital periods, enhances eccentricities, and produces measurable space velocities. We find that with reasonable initial conditions, it can self-consistently explain the formation of WR 140-like systems. The adopted parameters for the mass ejections are chosen to adhere to our current understanding of LBVs.

Our population synthesis calculations are based on a dense grid of detailed binary evolution models computed with the SMC metallicity (Wang et al. 2020; Xu et al. 2025b) and the WR+O population derived from it (Xu et al. 2025b). With the empirical eccentricity function in Sana et al. (2012) for the initial eccentricities of our model binaries, our Simulation1 predicts statistically 5.3 close WR+O binaries formed through the mass-transfer-driven orbital evolution, 3.8 wide WR+O binaries formed through the mass-ejection-driven orbital evolution, and 1.9 runaway WR stars, which well reproduce the observed WR star population in the SMC, 4 close WR+O binaries and 7 apparently single WR stars, including 2 runaways (Schootemeijer et al. 2024). The mass-ejection WR+O binaries would be difficult to identify observationally, due to their high eccentricities (0.4–1) and long orbital periods (peaking at 10^3 d). Hence, our scenario leads to WR binaries that are harder to identify as such in radial velocity studies. Notably, based on their increased orbital separations, they would be easier to find by GAIA. Given the uncertainties in the initial eccentricity function, the apparent absence of long-period WR+O binaries can also be explained by the binary disruption during the LBV stage if initially wide O star binaries are more eccentric than we assumed. Future detections of more WR 140-like systems, particularly in the Magellanic Clouds, will provide further insights into the evolution of initially wide O star binaries.

Whereas not explored in detail, we find that our scenario is also capable of providing progenitor evolution models for the systems Gaia BH1 and Gaia BH2, which consist of $\sim 10 M_{\odot}$ BHs with solar type stars in wide eccentric orbits (Sect. 4.4). It has implications for the formation of merging BBHs through the CEE channel (Sect. 4.3). If a WR star formed by mass-ejection-driven orbital evolution can produce a BH, our model predicts the existence of long-period and eccentric BH+O binaries. Such systems may experience further mass transfer in this eccentric configuration (Sepinsky et al. 2007, 2009; Rocha et al. 2025; Parkosidis et al. 2025a,b) or even a second phase of mass-ejection-driven orbital evolution. Merging BBHs can hardly be formed in either case. The CEE channel remains possible only if tides in long-period and eccentric BH+O binaries are strong enough to circularise the orbits.

Acknowledgements. X.-T.X. thanks Dong Lai and Abel Schootemeijer for helpful discussions. X.-T.X. was supported by the Tsung-Dao Lee postdoctoral fellowship at the Tsung-Dao Lee Institute (TDLI). This research was supported in part by grant NSF PHY-2309135 to the Kavli Institute for Theoretical Physics (KITP). X.-D.L. was supported by the National Key Research and Development Program of China (2021YFA0718500), the Natural Science Foundation of China under grant No. 12041301 and 12121003. A.H. was supported by the Australian Research Council (DP240101786, DP240103174) and by the Alexander von Humboldt Foundation.

References

- Abramowitz, M. & Stegun, I. A. 1972, *Handbook of Mathematical Functions* (National Bureau of Standards)
- Aguilera-Dena, D. R., Langer, N., Antoniadis, J., et al. 2022, *A&A*, 661, A60
- Aguilera-Dena, D. R., Müller, B., Antoniadis, J., et al. 2023, *A&A*, 671, A134
- Bavera, S. S., Fragos, T., Zapartas, E., et al. 2023, *Nature Astronomy*, 7, 1090
- Bavera, S. S., Fragos, T., Zevin, M., et al. 2021, *A&A*, 647, A153
- Belczynski, K., Holz, D. E., Bulik, T., & O’Shaughnessy, R. 2016, *Nature*, 534, 512
- Belczynski, K., Kalogera, V., Rasio, F. A., et al. 2008, *ApJS*, 174, 223
- Blaauw, A. 1961, *Bull. Astron. Inst. Netherlands*, 15, 265
- Bonačić Marinović, A. A., Glebbeek, E., & Pols, O. R. 2008, *A&A*, 480, 797
- Briel, M. M., Fragos, T., Gallegos-Garcia, M., et al. 2026, *arXiv e-prints*, arXiv:2602.03629
- Broekgaard, F. S., Stevenson, S., & Thrane, E. 2022, *ApJ*, 938, 45
- Campagnolo, J. C. N., Borges Fernandes, M., Drake, N. A., et al. 2018, *A&A*, 613, A33
- Chen, Z. 2025, *arXiv e-prints*, arXiv:2510.14173
- Cheng, S. J., Goldberg, J. A., Cantiello, M., et al. 2024, *ApJ*, 974, 270
- Corcoran, M. F., Ishibashi, K., Swank, J. H., & Petre, R. 2001, *ApJ*, 547, 1034
- Deshmukh, K., Sana, H., Mérand, A., et al. 2024, *A&A*, 692, A109
- Dsilva, K., Shenar, T., Sana, H., & Marchant, P. 2023, *A&A*, 674, A88
- Dzib, S. & Rodríguez, L. F. 2009, *Rev. Mexicana Astron. Astrofis.*, 45, 3
- El-Badry, K., Rix, H.-W., Cendes, Y., et al. 2023a, *MNRAS*, 521, 4323
- El-Badry, K., Rix, H.-W., Quataert, E., et al. 2023b, *MNRAS*, 518, 1057
- Eldridge, J. J., Stanway, E. R., Xiao, L., et al. 2017, *PASA*, 34, e058
- Foellmi, C., Moffat, A. F. J., & Guerrero, M. A. 2003, *MNRAS*, 338, 360
- Fragos, T., Andrews, J. J., Bavera, S. S., et al. 2023, *ApJS*, 264, 45
- Gaia Collaboration, Panuzzo, P., Mazeh, T., et al. 2024, *A&A*, 686, L2
- Gilkis, A. & Mazeh, T. 2024, *MNRAS*, 535, L44
- Gräfener, G. & Hamann, W.-R. 2008, *A&A*, 482, 945
- Gräfener, G., Owocki, S. P., & Vink, J. S. 2012, *A&A*, 538, A40
- Grassitelli, L., Langer, N., Mackey, J., et al. 2021, *A&A*, 647, A99
- Groh, J. H., Hillier, D. J., & Damineli, A. 2011, *ApJ*, 736, 46
- Hainich, R., Rühling, U., Todt, H., et al. 2014, *A&A*, 565, A27
- Henneco, J., Schneider, F. R. N., & Laplace, E. 2024, *A&A*, 682, A169
- Hillier, D. J., Davidson, K., Ishibashi, K., & Gull, T. 2001, *ApJ*, 553, 837
- Hills, J. G. 1983, *ApJ*, 267, 322
- Humphreys, R. M. & Davidson, K. 1994, *PASP*, 106, 1025
- Hurley, J. R., Tout, C. A., & Pols, O. R. 2002, *MNRAS*, 329, 897
- Iorio, G., Tornamenti, S., Mapelli, M., et al. 2024, *A&A*, 690, A144
- Ivanova, N., Justham, S., Chen, X., et al. 2013, *A&A Rev.*, 21, 59
- Janka, H.-T. 2017, *ApJ*, 837, 84
- Jin, H., Langer, N., Ercolino, A., & de Mink, S. E. 2025, *arXiv e-prints*, arXiv:2510.19965
- Jin, H., Langer, N., Lennon, D. J., & Proffitt, C. R. 2024, *A&A*, 690, A135
- Kashi, A. & Soker, N. 2018, *MNRAS*, 480, 3195

- Klencki, J., Podsiadlowski, P., Langer, N., et al. 2025, arXiv e-prints, arXiv:2505.08860
- Kotko, I., Banerjee, S., & Belczynski, K. 2024, MNRAS, 535, 3577
- Kozai, Y. 1962, AJ, 67, 591
- Kroupa, P. 2001, MNRAS, 322, 231
- Kruckow, M. U., Tauris, T. M., Langer, N., Kramer, M., & Izzard, R. G. 2018, MNRAS, 481, 1908
- Langer, N. 1987, A&A, 171, L1
- Langer, N. 2012, ARA&A, 50, 107
- Langer, N., Schürmann, C., Stoll, K., et al. 2020, A&A, 638, A39
- Lau, M. Y. M., Hirai, R., Mandel, I., & Tout, C. A. 2024, ApJ, 966, L7
- Lau, M. Y. M., Hirai, R., Price, D. J., Mandel, I., & Bate, M. R. 2025, A&A, 699, A274
- Lefèvre, L., Marchenko, S. V., Lépine, S., et al. 2005, MNRAS, 360, 141
- Lei, H., Circi, C., & Ortore, E. 2018, MNRAS, 481, 4602
- Lidov, M. L. 1962, Planet. Space Sci., 9, 719
- Mahy, L., Lanthermann, C., Hutsemékers, D., et al. 2022, A&A, 657, A4
- Mandel, I. & Broekgaarden, F. S. 2022, Living Reviews in Relativity, 25, 1
- Mapelli, M. 2020, Frontiers in Astronomy and Space Sciences, 7, 38
- Marchant, P. & Bodensteiner, J. 2024, ARA&A, 62, 21
- Marchant, P., Pappas, K. M. W., Gallegos-Garcia, M., et al. 2021, A&A, 650, A107
- Moe, M. & Di Stefano, R. 2017, ApJS, 230, 15
- Murray, C. D. & Dermott, S. F. 1999, Solar System Dynamics (Cambridge University Press)
- Naos, S., Haiman, Z., Quataert, E., & Holzkecht, L. 2025, ApJ, 992, L12
- Olejak, A., Klencki, J., Vigna-Gomez, A., et al. 2025, arXiv e-prints, arXiv:2511.10728
- Olejak, A., Klencki, J., Xu, X.-T., et al. 2024, A&A, 689, A305
- Parkosidis, A., Toonen, S., Dosopoulou, F., & Laplace, E. 2025a, arXiv e-prints, arXiv:2509.05243
- Parkosidis, A., Toonen, S., Laplace, E., & Dosopoulou, F. 2025b, arXiv e-prints, arXiv:2511.07190
- Pauli, D., Langer, N., Aguilera-Dena, D. R., Wang, C., & Marchant, P. 2022, A&A, 667, A58
- Pauli, D., Langer, N., Schootemeijer, A., et al. 2026, arXiv e-prints, arXiv:2601.08822
- Petrovic, J., Langer, N., & van der Hucht, K. A. 2005, A&A, 435, 1013
- Pfahl, E., Rappaport, S., & Podsiadlowski, P. 2002, ApJ, 573, 283
- Rastello, S., Iorio, G., Mapelli, M., et al. 2023, MNRAS, 526, 740
- Rocha, K. A., Hur, R., Kalogera, V., et al. 2025, The Astrophysical Journal, 983, 39
- Rosslove, C. K. & Crowther, P. A. 2015, MNRAS, 447, 2322
- Sana, H., de Koter, A., de Mink, S. E., et al. 2013, A&A, 550, A107
- Sana, H., de Mink, S. E., de Koter, A., et al. 2012, Science, 337, 444
- Sana, H., Shenar, T., Bodensteiner, J., et al. 2025, Nature Astronomy, 14
- Sanyal, D., Grassitelli, L., Langer, N., & Bestenlehner, J. M. 2015, A&A, 580, A20
- Sanyal, D., Langer, N., Szécsi, D., -C Yoon, S., & Grassitelli, L. 2017, A&A, 597, A71
- Scherbak, P., Lu, W., & Fuller, J. 2025, ApJ, 990, 172
- Schootemeijer, A. & Langer, N. 2018, A&A, 611, A75
- Schootemeijer, A., Shenar, T., Langer, N., et al. 2024, A&A, 689, A157
- Schürmann, C. & Langer, N. 2024, A&A, 691, A174
- Schürmann, C., Langer, N., Kramer, J. A., et al. 2024, A&A, 690, A282
- Schürmann, C., Xu, X.-T., Langer, N., et al. 2025, A&A, 704, A219
- Sen, K., Langer, N., Marchant, P., et al. 2022, A&A, 659, A98
- Sepinsky, J. F., Willems, B., Kalogera, V., & Rasio, F. A. 2007, ApJ, 667, 1170
- Sepinsky, J. F., Willems, B., Kalogera, V., & Rasio, F. A. 2009, ApJ, 702, 1387
- Shao, Y. & Li, X.-D. 2014, ApJ, 796, 37
- Shao, Y. & Li, X.-D. 2016, ApJ, 833, 108
- Shenar, T. 2024, arXiv e-prints, arXiv:2410.04436
- Shenar, T., Gilkis, A., Vink, J. S., Sana, H., & Sander, A. A. C. 2020, A&A, 634, A79
- Shenar, T., Hainich, R., Todt, H., et al. 2018, A&A, 616, A103
- Shenar, T., Hainich, R., Todt, H., et al. 2016, A&A, 591, A22
- Smith, N. 2014, ARA&A, 52, 487
- Smith, N. 2017a, MNRAS, 471, 4465
- Smith, N. 2017b, Philosophical Transactions of the Royal Society of London Series A, 375, 20160268
- Smith, N., Aghakhanloo, M., Murphy, J. W., et al. 2019, MNRAS, 488, 1760
- Smith, N., Andrews, J. E., Rest, A., et al. 2018, MNRAS, 480, 1466
- Smith, N. & Frew, D. J. 2011, MNRAS, 415, 2009
- Smith, N., Gehrz, R. D., Hinz, P. M., et al. 2003, AJ, 125, 1458
- Smith, N. & Hartigan, P. 2006, ApJ, 638, 1045
- Smith, N. & Owocki, S. P. 2006, ApJ, 645, L45
- Smith, N., Vink, J. S., & de Koter, A. 2004, ApJ, 615, 475
- Soker, N. 2000, A&A, 357, 557
- Strawn, E., Richardson, N. D., Moffat, A. F. J., et al. 2023, MNRAS, 519, 5882
- Tauris, T. M. & Takens, R. J. 1998, A&A, 330, 1047
- Tauris, T. M. & van den Heuvel, E. P. J. 2006, Formation and evolution of compact stellar X-ray sources, Vol. 39 (Cambridge University Press), 623–665
- Tauris, T. M. & van den Heuvel, E. P. J. 2023, Physics of Binary Star Evolution. From Stars to X-ray Binaries and Gravitational Wave Sources (Princeton University Press)
- Thomas, J. D., Richardson, N. D., Eldridge, J. J., et al. 2021, MNRAS, 504, 5221
- van den Heuvel, E. P. J., Portegies Zwart, S. F., Bhattacharya, D., & Kaper, L. 2000, A&A, 364, 563
- van den Heuvel, E. P. J., Portegies Zwart, S. F., & de Mink, S. E. 2017, MNRAS, 471, 4256
- Vanbeveren, D. 1991, A&A, 252, 159
- Verbunt, F. & Phinney, E. S. 1995, A&A, 296, 709
- Vinciguerra, S., Neijssel, C. J., Vigna-Gómez, A., et al. 2020, MNRAS, 498, 4705
- Vink, J. S. 2012, in Astrophysics and Space Science Library, Vol. 384, Eta Carinae and the Supernova Impostors, ed. K. Davidson & R. M. Humphreys, 221
- Vink, J. S. & de Koter, A. 2002, A&A, 393, 543
- von Zeipel, H. 1910, Astronomische Nachrichten, 183, 345
- Vos, J., Østensen, R. H., Marchant, P., & Van Winckel, H. 2015, A&A, 579, A49
- Wang, C., Bodensteiner, J., Xu, X.-T., et al. 2024, ApJ, 975, L20
- Wang, C., Langer, N., Schootemeijer, A., et al. 2020, ApJ, 888, L12
- Wang, C., Lau, M. Y. M., Li, X.-D., et al. 2026, arXiv e-prints, arXiv:2601.08508
- Willcox, R., Schneider, F. R. N., Laplace, E., et al. 2025, arXiv e-prints, arXiv:2510.07573
- Williams, P. M. 2019, MNRAS, 488, 1282
- Williams, P. M., Rauw, G., & van der Hucht, K. A. 2009, MNRAS, 395, 2221
- Wolf, B. 1989, A&A, 217, 87
- Xing, Z., Fragos, T., Kalogera, V., et al. 2026, arXiv e-prints [arXiv:2602.06259]
- Xu, X.-T. 2024, PhD thesis, University of Bonn, <https://bonndoc.ulb.uni-bonn.de/xmlui/handle/20.500.11811/11282>
- Xu, X.-T., Langer, N., Klencki, J., Wang, C., & Li, X.-D. 2025a, arXiv e-prints, arXiv:2512.20054
- Xu, X.-T., Schürmann, C., Langer, N., et al. 2025b, A&A, 704, A218
- Zapartas, E., Fox, O. D., Su, J., et al. 2025, arXiv e-prints, arXiv:2508.12677

Appendix A: Mass ejection at apastron

In the main text, we focus on the mass ejection at periastron. In this section, we extend the calculation to apastron for completeness. By replacing $r_{\text{per},0}$ by the separation at apastron, $r_{\text{ap},0}$, and $v_{\text{per},0}$ by the relative velocity at apastron,

$$v_{\text{ap},0} = \sqrt{\frac{GM_{\text{b},0}}{a_0} \frac{1-e_0}{1+e_0}} = \left(\frac{GM_{\text{b},0}}{P_{\text{orb},0}} 2\pi\right)^{1/3} \sqrt{\frac{1-e_0}{1+e_0}}, \quad (\text{A.1})$$

in the equations in Sect. (2.1), we can obtain the orbital parameters after the n th apastron passage, which are

$$a_n = a_0(1+e_0) \frac{M_{\text{b},0} - n\Delta M}{M_{\text{b},0}(1+e_0) - 2n\Delta M}, \quad (\text{A.2})$$

$$e_n^2 = \left(\frac{e_0 M_{\text{b},0} - n\Delta M}{M_{\text{b},0} - n\Delta M}\right)^2, \quad (\text{A.3})$$

$$P_{\text{orb},n}^2 = P_{\text{orb},0}^2 \frac{(1 - n\Delta M/M_{\text{b},0})^2 (1+e_0)^3}{[(1+e_0) - 2n\Delta M/M_{\text{b},0}]^3}, \quad (\text{A.4})$$

$$v_{\text{CoM},n} = \frac{n\Delta M M_{\text{s}2}}{M_{\text{b},0}(M_{\text{b},0} - n\Delta M)} v_{\text{ap},0}. \quad (\text{A.5})$$

Different from the periastron case, eccentricities have two solutions depending on ejected mass, which are

$$e_n = \begin{cases} (e_0 M_{\text{b},0} - n\Delta M)/(M_{\text{b},0} - n\Delta M) & \text{for } n\Delta M \leq e_0 M_{\text{b},0} \\ (n\Delta M - e_0 M_{\text{b},0})/(M_{\text{b},0} - n\Delta M) & \text{for } n\Delta M > e_0 M_{\text{b},0} \end{cases}. \quad (\text{A.6})$$

These two solutions lead to the following relations,

- $n\Delta M < e_0 M_{\text{b},0}$: $a_n(1+e_n) = a_0(1+e_0)$, which means that the separation at apastron of the post-mass-ejection orbit is equal to that of the pre-mass-ejection orbit;
- $n\Delta M > e_0 M_{\text{b},0}$: $a_n(1-e_n) = a_0(1+e_0)$, which means that the separation at periastron of the post-mass-ejection orbit is equal to that at apastron of the pre-mass-ejection orbit.

The orientation of the post-mass-ejection orbit also changes differently in both cases. The Laplace-Runge-Lenz vector before the mass ejection is

$$\vec{e}_0 = \left[\frac{v_{\text{ap},0}^2}{GM_{\text{b},0}} - \frac{1}{r_{\text{ap},0}} \right] \vec{r}_{\text{ap},0} = \frac{-e_0}{a_0(1+e_0)} \vec{r}_{\text{ap},0}, \quad (\text{A.7})$$

and, after ejecting $n\Delta M$ mass, it becomes

$$\vec{e}_1 = \left[\frac{v_{\text{ap},0}^2}{G(M_{\text{b},0} - n\Delta M)} - \frac{1}{r_{\text{ap},0}} \right] \vec{r}_{\text{ap},0}. \quad (\text{A.8})$$

Taking $n\Delta M = e_0 M_{\text{b},0}$ leads to

$$\frac{v_{\text{ap},0}^2}{G(M_{\text{b},0} - e_0 M_{\text{b},0})} - \frac{1}{r_{\text{ap},0}} = 0. \quad (\text{A.9})$$

Therefore,

- $n\Delta M < e_0 M_{\text{b},0}$: $\vec{e}_0 \cdot \vec{e}_1 = |\vec{e}_0 \cdot \vec{e}_1|$, which means that the orientation of apastron of the pre-mass-ejection orbit is the same as for the post-mass-ejection orbit;
- $n\Delta M > e_0 M_{\text{b},0}$: $\vec{e}_0 \cdot \vec{e}_1 = -|\vec{e}_0 \cdot \vec{e}_1|$, which means that the orientation of apastron of the pre-mass-ejection orbit becomes the orientation of periastron of the post-mass-ejection orbit.

Appendix B: Establishing the formulae in Sect. 2.1.3 using mathematical induction

Theorem. After the n th mass ejection at periastron, the orbital parameters are given by

$$a_n = a_0(1 - e_0) \frac{M_{b,0} - n\Delta M}{M_{b,0}(1 - e_0) - 2n\Delta M}, \quad (\text{B.1})$$

$$e_n = \frac{n\Delta M + e_0 M_{b,0}}{M_{b,0} - n\Delta M}, \quad (\text{B.2})$$

$$P_{\text{orb},n}^2 = P_{\text{orb},0}^2 \frac{(1 - n\Delta M/M_{b,0})^2(1 - e_0)^3}{[(1 - e_0) - 2n\Delta M/M_{b,0}]^3}, \quad (\text{B.3})$$

$$v_{\text{CoM},n} = \frac{n\Delta M M_{s2}}{M_{b,0}(M_{b,0} - n\Delta M)} v_{\text{per},0}. \quad (\text{B.4})$$

Proof. We establish the formulae by induction on n .

– **Base case.** Taking $n = 1$, Eqs. (B.1)-(B.4) are consistent with our result for one periastron passage (Sect. 2.1.2).

– **Inductive hypothesis.** We assume that the identity of Eqs. (B.1)-(B.4) holds for a given number of periastron passage, k , which is

$$a_k = a_0(1 - e_0) \frac{M_{b,0} - k\Delta M}{M_{b,0}(1 - e_0) - 2k\Delta M}, \quad (\text{B.5})$$

$$e_k = \frac{k\Delta M + e_0 M_{b,0}}{M_{b,0} - k\Delta M}, \quad (\text{B.6})$$

$$P_{\text{orb},k}^2 = P_{\text{orb},0}^2 \frac{(1 - k\Delta M/M_{b,0})^2(1 - e_0)^3}{[(1 - e_0) - 2k\Delta M/M_{b,0}]^3}, \quad (\text{B.7})$$

$$v_{\text{CoM},k} = \frac{k\Delta M M_{s2}}{M_{b,0}(M_{b,0} - k\Delta M)} v_{\text{per},0}. \quad (\text{B.8})$$

– **Inductive step.** In the following, we show that this identity holds for $n = k + 1$. After the k th periastron passage, the total mass of the binary becomes $(M_{b,0} - k\Delta M)$, and the mass ejected during the $(k + 1)$ th periastron passage is ΔM according to our assumption. The orbital parameters after the $(k + 1)$ th periastron passage, $(a_{k+1}, e_{k+1}, P_{\text{orb},k+1}, v_{\text{CoM},k+1})$, can be obtained by using our result for one mass ejection, Eqs. (24)-(26) and (29). By replacing the pre-mass-ejection binary mass, $M_{b,0}$, by $(M_{b,0} - k\Delta M)$, we obtain

$$a_{k+1} = a_k(1 - e_k) \frac{(M_{b,0} - k\Delta M) - \Delta M}{(M_{b,0} - k\Delta M)(1 - e_k) - 2\Delta M} = a_0(1 - e_0) \frac{[M_{b,0} - (k + 1)\Delta M]}{M_{b,0}(1 - e_0) - 2(k + 1)\Delta M}, \quad (\text{B.9})$$

$$e_{k+1} = \frac{\Delta M + e_k(M_{b,0} - k\Delta M)}{(M_{b,0} - k\Delta M) - \Delta M} = \frac{(k + 1)\Delta M + e_0 M_{b,0}}{M_{b,0} - (k + 1)\Delta M}, \quad (\text{B.10})$$

$$P_{\text{orb},k+1}^2 = P_{\text{orb},k}^2 \frac{[1 - \Delta M/(M_{b,0} - k\Delta M)]^2(1 - e_k)^3}{[(1 - e_k) - 2\Delta M/(M_{b,0} - k\Delta M)]^3} = P_{\text{orb},0}^2 \frac{[1 - (k + 1)\Delta M/M_{b,0}]^2(1 - e_0)^3}{[(1 - e_0) - 2(k + 1)\Delta M/M_{b,0}]^3}, \quad (\text{B.11})$$

$$v_{\text{CoM},k+1} = v_{\text{CoM},k} + \frac{\Delta M M_{s2}}{(M_{b,0} - k\Delta M)[(M_{b,0} - \Delta M) - k\Delta M]} v_{\text{per},0} = \frac{(k + 1)\Delta M M_{s2}}{M_{b,0}[M_{b,0} - (k + 1)\Delta M]} v_{\text{per},0}. \quad (\text{B.12})$$

These equations are consistent with the expectation of Eqs. (B.1)-(B.4) by taking $n = k + 1$.

– **Conclusion.** we conclude that Eqs. (B.1)-(B.4) hold for all positive integer n if the binary stays bound (i.e., $e_n < 1$).

Appendix C: WR 140: MESA fitting method

We scanned through the comprehensive binary evolution model grid of Jin et al. (2025) to search for the MESA binary models matching the observed properties of WR 140 and its companion. We required the models to satisfy the following three constraints simultaneously:

- the system undergoes Case B mass transfer;
- after mass transfer, the primary becomes a stripped star (WR star) with a mass of $10.31 \pm 0.45 M_{\odot}$ during its core helium burning phase, and it would appear as a WC star with a surface carbon mass fraction above 0.2;
- the secondary is an O-type star with a mass of $29.27 \pm 1.14 M_{\odot}$.

Since the MESA models were computed assuming stable mass transfer in circular orbits, we did not impose any constraints on the orbital periods and eccentricities of the models. We find that models with an initial primary mass of about $40 M_{\odot}$, an initial mass ratio close to 1 (i.e., initial secondary masses of $30\text{--}35 M_{\odot}$), and initial orbital periods in a range of about $200\text{--}300$ d could satisfy all the three constraints simultaneously. These binary models would appear as WC+O binaries for a few 0.1 Myr, which is a significant fraction of the core helium burning timescale of the primary stars.

Appendix D: Predictions with fixed initial eccentricities

In this section, we present the population synthesis predictions with fixed initial eccentricities, 0.0, 0.1, 0.2, 0.3, and 0.5 (Fig. D.1). Consistent with the fiducial population synthesis model, M_{crit} and P_{crit} are taken to be $30 M_{\odot}$ and 40 d. Predictions with initial eccentricities above 0.6 are not presented, since all the systems entering the mass-ejection-driven orbital evolution are disrupted.

With the increasing of initial eccentricities, the orbital periods of the mass-ejection WR+O binaries are shifted towards the long-period regime. Binary disruption starts to take place with $e_0 = 0.3$. Correspondingly, the expected eccentricities also increase from ~ 0.5 to near 1, while the velocities of the centre of mass stay at around 20–40 km s⁻¹.

Appendix E: Predictions by different population synthesis models

In this section, we present the distribution functions derived from the High- M_{crit} , High- P_{crit} , and Flat- f_e models (see Tab. 2 for the definitions of the models). The predicted populations are presented in Fig. E.1. We refer to Sect. 3.3.3 for detailed descriptions.

Appendix F: Apsidal advance

In the main text, we have ignored the effects of apsidal advance, which can significantly reduce the velocity of the centre of mass by changing the angle between $\vec{v}_{\text{per},0}$ and $\vec{v}_{\text{CoM},0}$ in Eq. (28). In this section, we estimate the effect of apsidal advance by assuming that the periastron rotates at a fixed angular momentum velocity, ω_{ap} .

Considering a coordinate system corotating with the orbit, the X-axis has the opposite direction as the relative velocity at periastron, and the Y-axis points from the companion star to the mass-losing star (Fig. F.1). After the n th periastron passage, the velocity of the centre of mass and orbital period are defined as $\vec{v}_{\text{CoM},n}$ and $P_{\text{orb},n}$. We denote the components on the X- and Y-axis of $\vec{v}_{\text{CoM},n}$ as $v_{\text{CoM},n,x}$ and $v_{\text{CoM},n,y}$, respectively. In the following, we derive the velocity of the centre of mass, $v_{\text{CoM},n+1}$, after the $(n+1)$ th periastron passage by taking into account apsidal advance. Due to apsidal advance, the orientation of $\vec{v}_{\text{CoM},n}$ changes an angle of θ_n , which is

$$\theta_n = -\omega_{\text{ap}} P_{\text{orb},n}, \quad (\text{F.1})$$

where the negative sign is caused by the choice of the corotating coordinate system. For example, if the orientation of the orbit rotates clockwise for a faraway observer, $\vec{v}_{\text{CoM},n}$ should rotate anti-clockwise in this corotating coordinate system. Then, at the $(n+1)$ th mass ejection, $\vec{v}_{\text{CoM},n}$ becomes

$$\vec{v}_{\text{CoM},n} = \begin{bmatrix} v_{\text{CoM},n,x} \cos \theta_n - v_{\text{CoM},n,y} \sin \theta_n \\ v_{\text{CoM},n,x} \sin \theta_n + v_{\text{CoM},n,y} \cos \theta_n \end{bmatrix}. \quad (\text{F.2})$$

Let \vec{v}_{K} be the kick velocity induced by the $(n+1)$ th mass ejection, and the velocity of the centre of mass after the $(n+1)$ th mass ejection be given by

$$\vec{v}_{\text{CoM},n+1} = \vec{v}_{\text{CoM},n} + \vec{v}_{\text{K}}. \quad (\text{F.3})$$

As we have shown in Sect. 2.1.2, the direction of \vec{v}_{K} is the opposite direction of the relative velocity at periastron, which is (1, 0) in the considered coordinate system. Hence \vec{v}_{K} is given by

$$\vec{v}_{\text{K}} = \frac{\Delta M M_{s2}}{(M_{b,0} - n\Delta M)[(M_{b,0} - n\Delta M) - \Delta M]} v_{\text{per},0} \begin{bmatrix} 1 \\ 0 \end{bmatrix}, \quad (\text{F.4})$$

where $(M_{b,0} - n\Delta M)$ represents the total mass of the binary after the n th mass ejection. Combining Eqs. (F.2), (F.3), and (F.4), we obtained the X- and Y-axis components, $v_{\text{CoM},n+1,x}$ and $v_{\text{CoM},n+1,y}$, of $\vec{v}_{\text{CoM},n+1}$ as the following

$$v_{\text{CoM},n+1,x} = \left| (v_{\text{CoM},n,x} \cos \theta_n - v_{\text{CoM},n,y} \sin \theta_n) + \frac{\Delta M M_{s2}}{(M_{b,0} - n\Delta M)[(M_{b,0} - n\Delta M) - \Delta M]} v_0 \right|, \quad (\text{F.5})$$

and

$$v_{\text{CoM},n+1,y} = \left| (v_{\text{CoM},n,x} \sin \theta_n + v_{\text{CoM},n,y} \cos \theta_n) \right|. \quad (\text{F.6})$$

Then, we have

$$(v_{\text{CoM},n+1})_{\text{ap}} = \sqrt{v_{\text{CoM},n+1,x}^2 + v_{\text{CoM},n+1,y}^2}. \quad (\text{F.7})$$

In the following, we recalculate the velocities of the centre of mass, $v_{\text{CoM},\text{ap}}$, for the example models presented in Fig. 3 with the orbital orientation rotating at a constant angular velocity of

$$\omega_{\text{ap}} = \frac{2\pi}{10^4 P_{\text{orb},0}}. \quad (\text{F.8})$$

Our result is presented in Fig. F.2, where all models end up with $v_{\text{CoM},\text{ap}} \lesssim 5 \text{ km s}^{-1}$. Binaries cannot have considerable space velocities even if ω_{ap} is small. Hence the predicted velocity of the centre of mass should generally be treated as an upper limit.

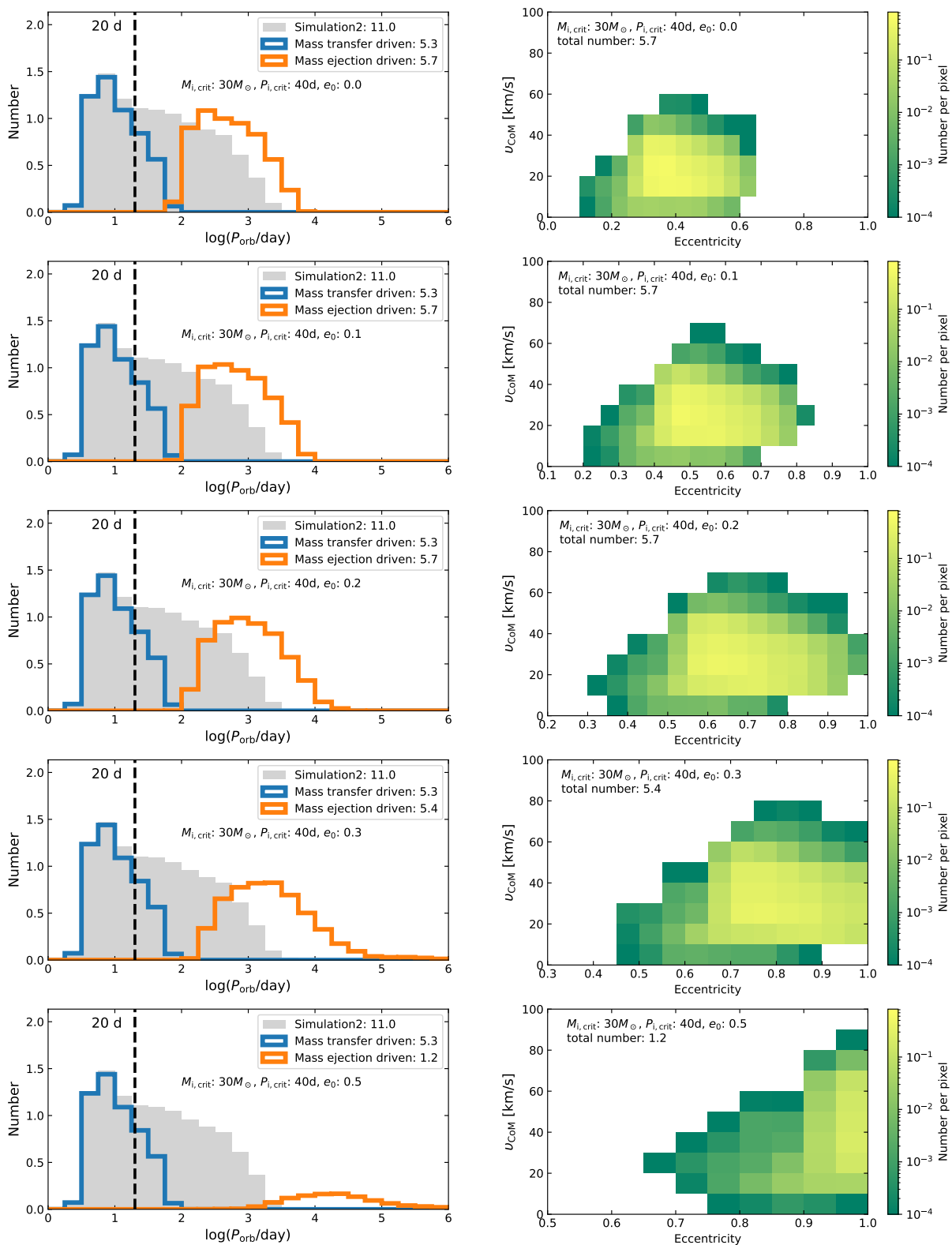


Fig. D.1. Population synthesis predictions with fixed initial eccentricities, which are 0.0, 0.1, 0.2, 0.3, and 0.5, from top to bottom. The left column shows the predicted orbital period distributions of the mass-transfer WR+O binaries (blue) and mass-ejection WR+O binaries (orange), where the predicted numbers are indicated in the text. The vertical lines correspond to the observed longest orbital period of the SMC WR+O binaries. The grey background is the prediction of Simulation2, which is the fiducial model in Xu et al. (2025b) but with a higher star formation rate. The right column shows the predicted population of the mass-ejection WR+O binaries on the eccentricity- u_{CoM} plane, where the predicted number in each pixel is colour-coded.

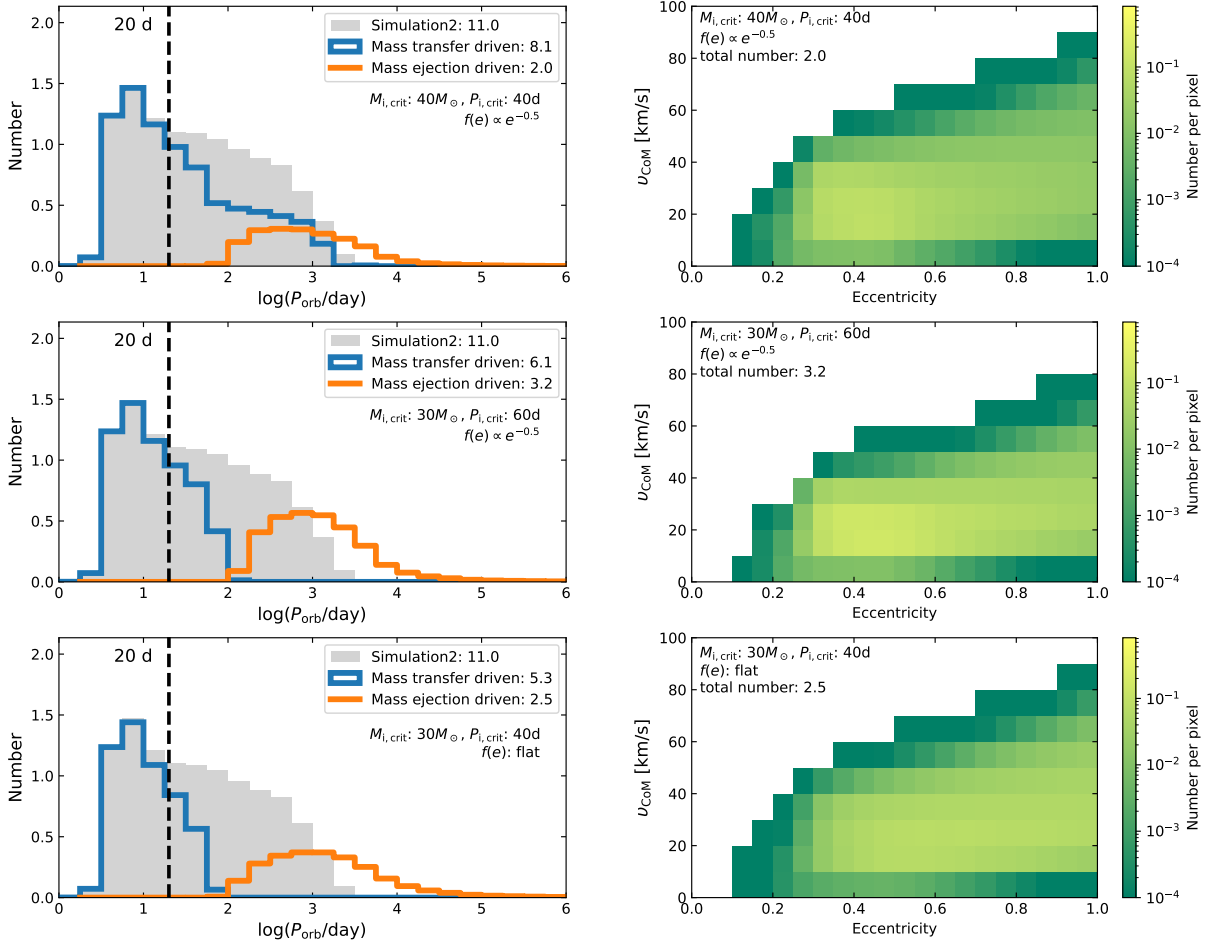


Fig. E.1. Predicted populations by different population synthesis models. The colours and legends have the same meaning as in Fig. D.1. From top to bottom rows, we present the predictions in the High- M_{crit} model ($M_{\text{crit}} = 40 M_{\odot}$), High- P_{crit} model ($P_{\text{crit}} = 60$ d), and Flat- f_e model ($\eta = 0$).

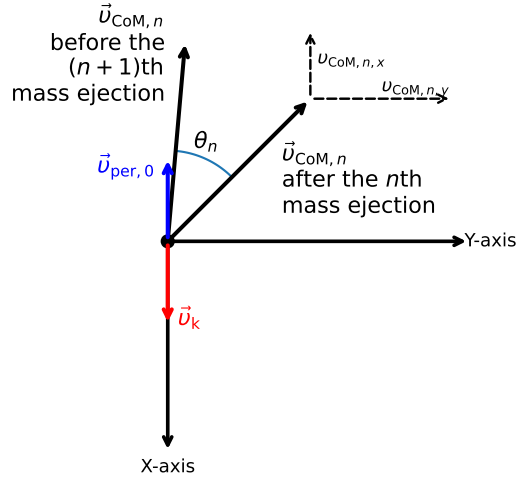


Fig. E.1. Coordinate system adopted for estimating the effect of apsidal advance on the velocity of centre of mass. Due to apsidal advance, the orientation of the velocity of the centre of mass, $\vec{v}_{\text{CoM},n}$, changes by an angle of θ_n from the n th to $(n+1)$ th mass ejection. The momentum kick induced by the $(n+1)$ th mass ejection, \vec{v}_k , has the opposite direction as the relative velocity at periastron, $\vec{v}_{\text{per},0}$.

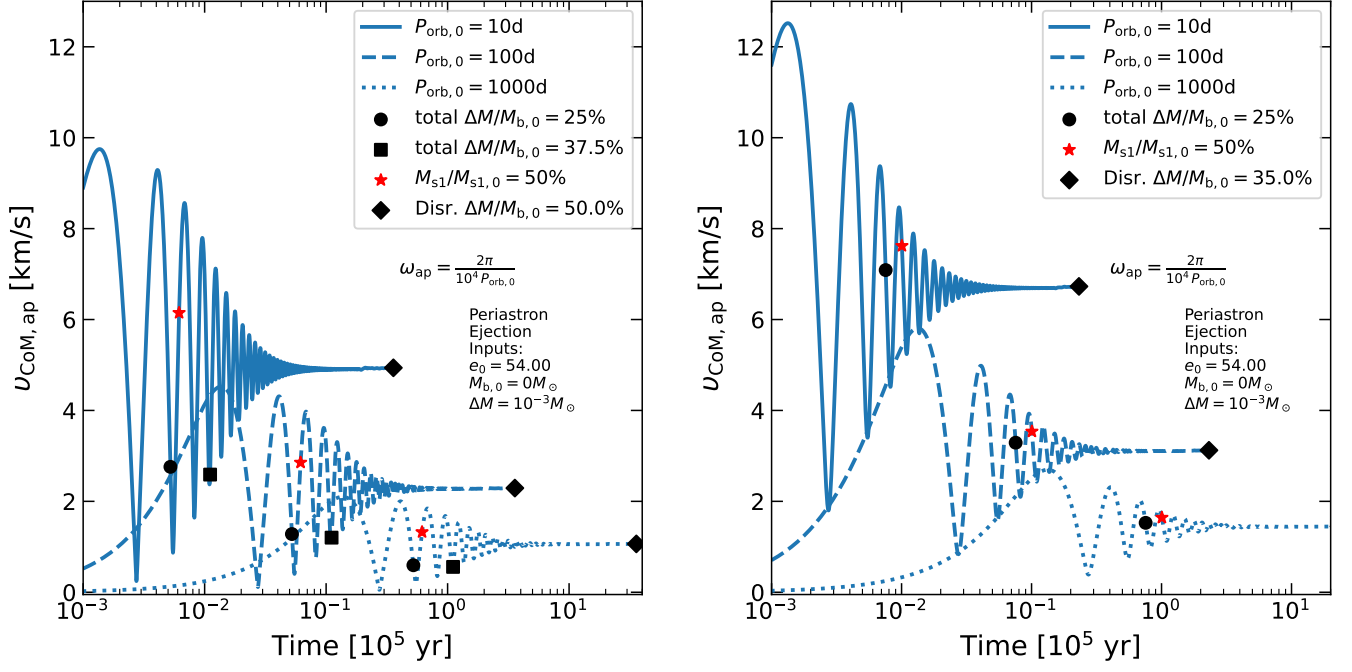


Fig. F.2. Effect of apsidal advance on the velocity of the centre of mass of the example models in Fig. 3. The apsidal advance angular velocity was taken to be $\omega_{\text{ap}} = 2\pi (10^4 P_{\text{orb},0})^{-1}$. The two panels correspond to two initial eccentricities, 0.0 (left) and 0.3 (right). Each panel contains three curves, computed with different initial orbital periods, 10 d (solid line), 100 d (dashed line), and 1000 d (dotted line). The markers indicate the points where the systems eject $25\%M_{b,0}$ (circle), $37.5\% M_{\odot}$ (square), and ΔM_{dis} (Eq. 30; diamond). The red star means that the mass-losing star ejects half of its initial mass.